Sedimentary Geothermal Feasibility Study

October 2016

Chad Augustine
National Renewable Energy Laboratory
Golden, Colorado

Luis Zerpa
Colorado School of Mines
Golden, Colorado

Sedimentary Geothermal Feasibility Study

October 2016

Chad Augustine
National Renewable Energy Laboratory
Golden, Colorado

Luis Zerpa
Colorado School of Mines
Golden, Colorado

NREL is a national laboratory of the U.S. Department of Energy
Office of Energy Efficiency & Renewable Energy
Operated by the Alliance for Sustainable Energy, LLC

This report is available at no cost from the National Renewable Energy Laboratory (NREL) at www.nrel.gov/publications.

National Renewable Energy Laboratory
15013 Denver West Parkway
Golden, CO 80401
303-275-3000 • www.nrel.gov

Subcontract Report
NREL/SR-6A20-66552
January 2017

Contract No. DE-AC36-08GO28308

NOTICE

This report was prepared as an account of work sponsored by an agency of the United States government. Neither the United States government nor any agency thereof, nor any of their employees, makes any warranty, express or implied, or assumes any legal liability or responsibility for the accuracy, completeness, or usefulness of any information, apparatus, product, or process disclosed, or represents that its use would not infringe privately owned rights. Reference herein to any specific commercial product, process, or service by trade name, trademark, manufacturer, or otherwise does not necessarily constitute or imply its endorsement, recommendation, or favoring by the United States government or any agency thereof. The views and opinions of authors expressed herein do not necessarily state or reflect those of the United States government or any agency thereof.

Cover Photos by Dennis Schroeder: (left to right) NREL 26173, NREL 18302, NREL 19758, NREL 29642, NREL 19795.

NREL prints on paper that contains recycled content.

Executive Summary

The objective of this project is to analyze the feasibility of commercial geothermal projects using numerical reservoir simulation, considering a sedimentary reservoir with low permeability that requires productivity enhancement. A commercial thermal reservoir simulator (STARS, from Computer Modeling Group, CMG) is used in this work for numerical modeling. In the first stage of this project (FY14), a hypothetical numerical reservoir model was developed, and validated against an analytical solution. The following model parameters were considered to obtain an acceptable match between the numerical and analytical solutions: grid block size, time step and reservoir areal dimensions; the latter related to boundary effects on the numerical solution. Systematic model runs showed that insufficient grid sizing generates numerical dispersion that causes the numerical model to underestimate the thermal breakthrough time compared to the analytic model. As grid sizing is decreased, the model results converge on a solution. Likewise, insufficient reservoir model area introduces boundary effects in the numerical solution that cause the model results to differ from the analytical solution.

In this report summarizing FY15 work, a more realistic geologic model is considered, developed using actual well log and core data from the selected target sedimentary formation. In this report we present the process of reservoir characterization of the Lyons sandstone formation of the Wattenberg field in Colorado. The reservoir characterization involved the pre-processing and analysis of 14 well logs, obtained from the Colorado Oil and Gas Conservation Commission website that were drilled through the Lyons formation. A geostatistical approach was used, based on the well log data, to construct a reservoir model with geologic features, such as, geometry (tops, bottom, and thickness), rock properties (i.e., porosity), and temperature. In addition, core measurement data was used to build a correlation between porosity and permeability. Three models (i.e., base case, object-based model, and dual permeability model) are presented to show how different geologic features affect the thermal behavior of the sedimentary geothermal system.

This report is available at no cost from the National Renewable Energy Laboratory (NREL) at www.nrel.gov/publications.

TABLE OF CONTENTS

LIST OF FIGURES

3

4

LIST OF TABLES

1 Reservoir characterization of the selected target sedimentary formation

In an effort to examine the feasibility of geothermal energy production from a sedimentary formation, the Lyons sandstone formation of the Wattenberg Field in Colorado was chosen for further simulation study. It is well known that the Wattenberg Field has a geothermal potential with high geothermal gradient (Morgan et al., 2009). The Lyons formation located at the depth of about 9,000 ft is being used for wastewater disposal, which indicates that the formation is likely to have favorable injectivity. In addition, we were readily able to collect actual well log data from a public domain: the Colorado Oil and Gas Information System (COGIS: http://cogcc.state.co.us/cogis/) thanks to the abundant oil and gas development activities in the Wattenberg Field.

1.1. Wattenberg field geology overview

The Permian Lyons Sandstone in the areas of the Wattenberg field (Figure 1-1) is our target formation for preliminary reservoir simulation. The lithofacies and the stratigraphy of the formation are shown in Figure 1-2. Some of the key features of the Lyons formations are listed as follows,

- Well-sorted fine sand
- Old sand dunes
- Main building material for CU-Boulder
- Sea began to creep in from the east
- Arid to west
- The middle Lyons Sandstone is easily eroded and forms a valley between the more resistant lower and upper units.

6
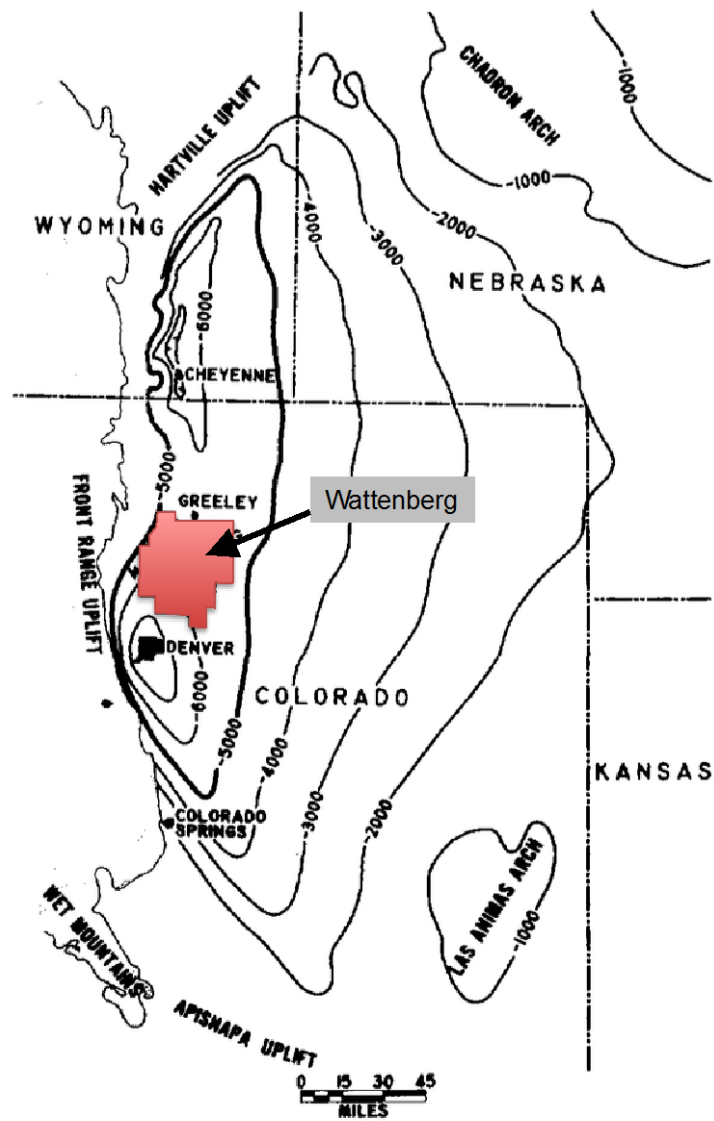
Figure 1-1. Location of Denver Basin, with Wattenberg field highlighted (Matuszczak, 1973).

	NORTHERN FRONT RANGE, OUTCROP	ADJACENT DENVER BASIN
QUAT.	Undifferentiated alluvial deposits	Undifferentiated alluvial deposits
TERTIARY	Undifferentiated boulder & gravel deposits	Castle Rock Conglomerate
	Denver Formation	Dawson-Denver Formations
UPPER CRETACEOUS	Arapahoe Formation	Arapahoe Formation
	Laramie Formation	Laramie Formation
	Fox Hills Sandstone	Fox Hills Sandstone
	Pierre Shale — Richard Sandstone Mbr.	Pierre Shale — Terry "Sussex" Ss. Member
	Terry Sandstone Mbr.	Hygiene "Shannon" Ss. Member
	Hygiene Sandstone Mbr.	Sharon Springs Member
	Niobrara Formation — Smoky Hill Shale Mbr.	Niobrara Formation — Smoky Hill Shale Member
	Fort Hays Limestone Mbr.	Fort Hays Limestone Member
	Codell Sandstone Mbr.	Codell Sandstone Member
	Carlile Shale	Carlile Shale
	Greenhorn Limestone	Greenhorn Limestone
	Graneros Shale	Graneros Shale — "D" sandstone
	Mowry Shale	Mowry Shale equivalent
LOWER CRETACEOUS	Dakota Group — South Platte Fm. — South: Upper members, South Platte Formation / North: Muddy ("J") Sandstone	Muddy ("J") Sandstone
	Skull Creek Shale	Skull Creek Shale
	Plainview Ss. Member / Plainview Formation	"Dakota" of drillers
	Lytle Formation	"Lakota" of drillers
JURASSIC	Morrison Formation	Morrison Formation
	Ralston Creek Formation	Older Jurassic rocks may be present
	Sundance Formation	
TRI.	Jelm Formation	Jelm Formation
PERMIAN	Lykins Formation	Lykins Formation
	Lyons Sandstone	Lyons Sandstone
	Owl Canyon Formation	Owl Canyon Formation
	Ingleside Formation	Ingleside Formation
PENNSYL-VANIAN	Fountain Formation	Fountain Formation
MISS.		Mississippian rocks
DEV.		Devonian rocks
SIL.		
ORD.		Ordovician rocks
CAM.		Cambrian rocks
PRE-CAM.	Metamorphic and intrusive rocks	

Figure 1-2. Stratigraphic section of rock units in outcrop and the adjacent Denver Basin - The Permian Lyons Sandstone formation is between Lykins and Owl Canyon formation (Higley and Cox, 2007).

8

1.2. Well log data and geothermal gradient

The wells considered for the construction of the Lyons formation model are located in Weld county, 70 km north of Denver, as shown in Figure 1-3. Data from 12 water disposal wells was collected from well log information from the Colorado Oil and Gas Conservation Commission (COGCC) website. Table 1-1 summarizes the well log data collected. The wells, drilled through the Lyons formation - a target water producing formation in this study, were selected. The well log data for wells #3, #4, #5, #6, and #7 were converted from an image file type to LAS (Log ASCII Standard), so that they could be loaded into the geologic software to build a geologic and geostatistical model for the reservoir simulator.
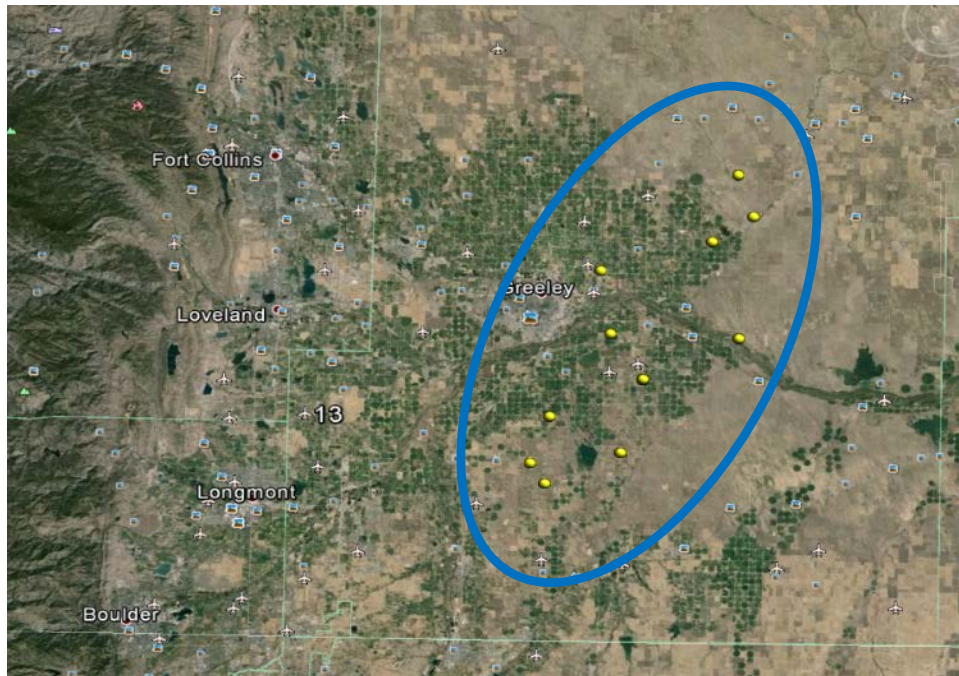
Figure 1-3. Locations of 12 water disposal wells in the Wattenberg field, in Colorado.

The top and bottom of the Lyons formation are identified from well information on COGIS. Taking well #1 for example, from the COGIS well information, the top and bottom of Lyons formation are at a depth of 8,742 ft and 8,898 ft, respectively. In the well log shown in Figure 1-4, a shaly sandstone layer with unstable resistivity measurements is identified above the Lyons formation, within a depth interval of 8,692 to 8,742 ft. For our modeling work, the upper shaly sandstone layer identified in the log is considered as a flow unit. The log tracks for all the wells are listed in Table A 1, in APPENDIX A (Well log analysis). The rock layer underneath the Lyons formation is identified as a shale bed rock formation that acts as a flow barrier or seal.

Therefore, the water producing formation includes the upper shaly sandstone layer and the Lyons formation identified from the COGIS well information.
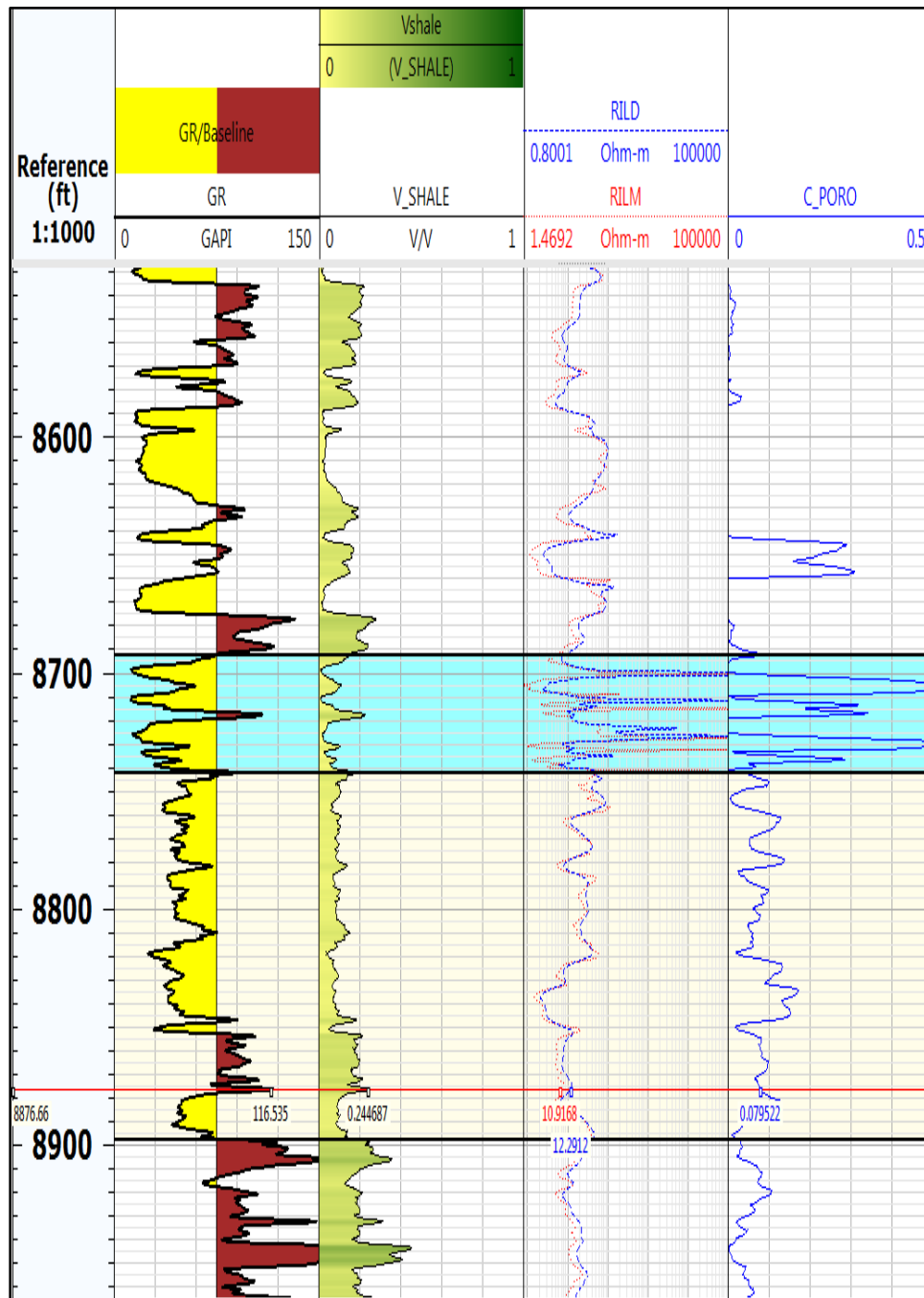
Figure 1-4. Log tracks for Well #1: gamma ray, shale volume, resistivity and calculated porosity.

The geothermal gradient is calculated based on the bottomhole temperature (BHT) data recorded in well log headers. A linear interpolation of surface temperature and bottomhole temperature is used to obtain the geothermal gradient values presented in Table 1-1. The surface temperature is

10

assumed to be 15 °C. The estimated geothermal gradient ranges from 25.5 °C/km to 46.8 °C/km with an average of 37.2 °C/km. Considering the fact that the normal geothermal gradient range from 25 to 30 °C/km, the area we are targeting has a high geothermal potential.

Table 1-1. Well log data: Tops, geothermal gradient and temperature at the top of Lyons formation

#	Well ID	Data Type	Upper Sandstone Layer (top) (ft)	Lyons Top (ft)	Lyons Bottom (ft)	Calculated Geothermal gradient (°C/km)	Calculated Temperature at Lyons top (°C)
W1	05-123-30367	LAS	8692	8742	8898	34.9	105.6
W2	05-123-26004	LAS	8956	9004	9148	36.3	112.1
W3	05-123-29168	TIF	9110	9164	9296	37.9	118.4
W4	05-123-16804	TIF	8579	8639	9022	35.9	107.1
W5	05-123-29536	TIF	8593	8654	8790	49.5	143.1
W6	05-123-19688	TIF	9000	9055	9184	45.8	139.0
W7	05-123-27116	LAS	8642	8696	8834	50.1	145.5
W8	05-123-25694	LAS	8479	8528	8638	48.1	137.7
W9	05-123-35841	LAS	8995	9050	9150	43.2	131.8
W10	05-123-32207	LAS	8455	8508	8645	42.0	121.5
W11	05-123-15685	TIF	8582	8630	8770	36.7	109.2
W12	05-123-23332	TIF	8108	8158	8244	42.6	118.5

2 Static Reservoir Model

The Lyons formation in the Wattenberg field, Denver-Julesburg Basin, was chosen as the candidate geothermal reservoir for this study. A static reservoir model was developed, with analysis of available formation data, such as well logs, bottomhole temperature, porosity and permeability from core samples. Then the ''sweet spot'' with high porosity and relatively high temperature was extracted out as the area of research, to perform reservoir simulations. This section describes the procedures followed during the generation of the static reservoir model.

2.1 Formation top and bottom

Based on the well log analysis (APPENDIX A), four different formations are identified. The Lyons formation consists of clean sandstone with relatively low shale volume. It is thought to be a water-bearing zone as it shows low resistivity values. Above this sandstone formation, shale cap rock forms a flow barrier. There is a sandstone layer right above the Lyons formation. It exhibits transitional characteristics with unstable resistivity values. A shale bedrock formation is identified below the Lyons formation. Therefore, our reservoir model includes the upper sandstone (UT) and the Lyons formation (LT), bounded by the shale cap and bedrock formations. We define two facies as flow units for our reservoir model.

2.2 Surface map and grid generation

The surface maps connecting the tops and bottoms are generated using Ordinary Kriging[1]. CMG built-in geostatistical tool allows users to implement Ordinary Kriging by providing a way to match a variogram[2] to the data, as shown in Figure 2-1. Figure 2-2 shows three contour maps for UT top, LT top and LT bottom generated through this geostatistical method. For the sake of computational efficiency, a grid-block size of 400 by 400 meters was chosen to cover the entire area that contains the 12 wells. The areal extent covering the 12 wells is 27,400 by 44,000

---

[1] Kriging is one of the most widely used geostatistical methods that estimates an unknown property at a location of interest by the weighted combination of known properties nearby.

[2] Variogram is defined as the average of squared value of difference in data at a certain location, showing a spatial correlation of data.

12

meters. The surface maps are shown in Figure 2-3. In this figure, the depth is with reference to the mean sea level.
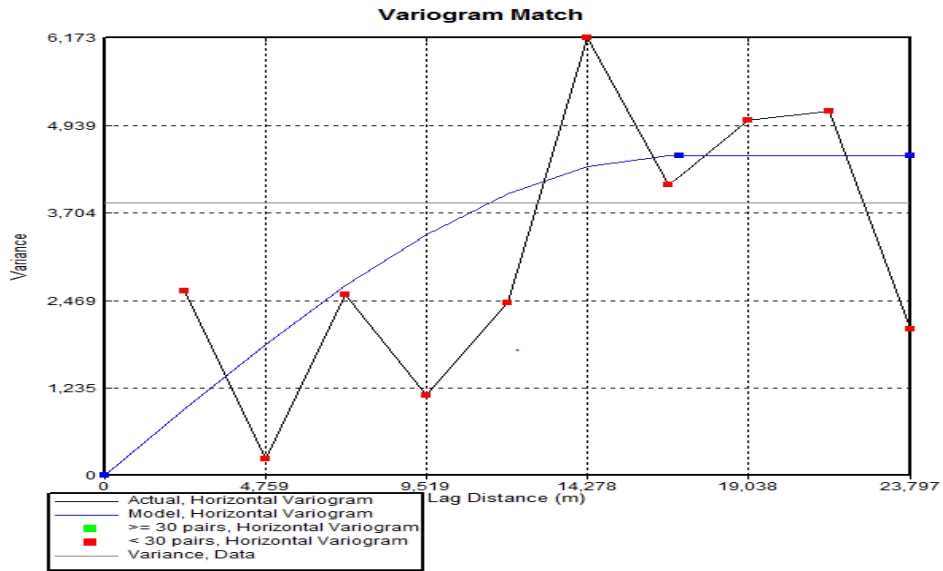
Figure 2-1. Variogram matching for surface maps.
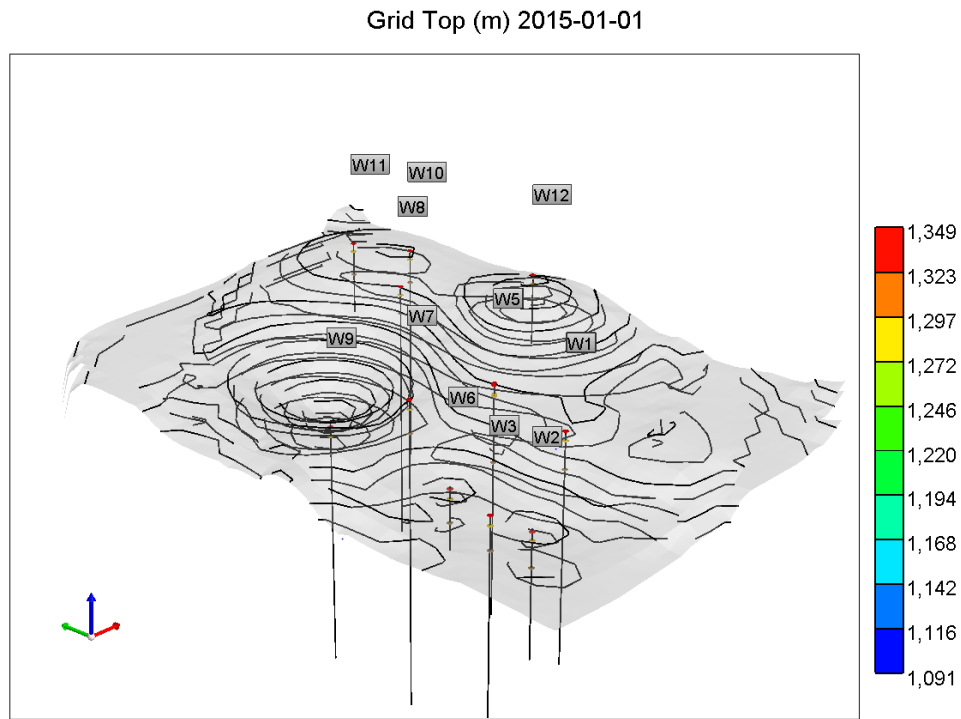
Grid Top (m) 2015-01-01

Figure 2-2. Surface maps generated using Ordinary Kriging.

13
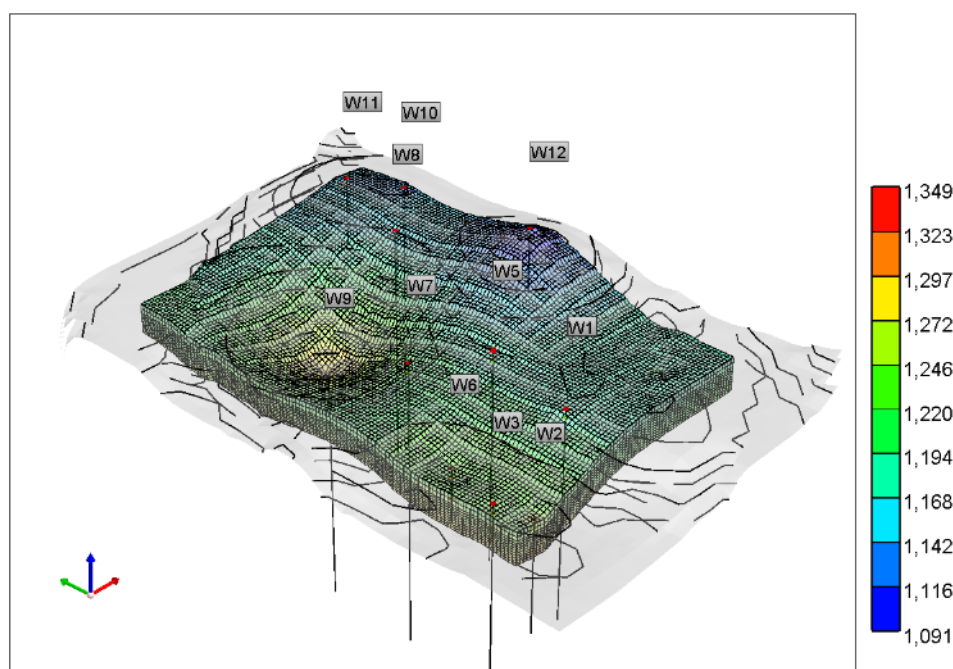
Figure 2-3. Numerical grid, with horizontal resolution of 400 by 400 m, and three surface maps for each formation boundaries.

2.3   Generation of reservoir properties

The porosity was calculated from the well log data using density porosity (DPOR) and neutron porosity (NPOR) logs. A quadratic mean was used to calculate the porosity based on well log measurements,

$$Porosity = \sqrt{\frac{DPOR^2 + NPOR^2}{2}} \qquad\qquad (2.1)$$

For the well logs that do not present values for DPOR or NPOR, the available value for porosity was used as the reservoir porosity value. Negative values for DPOR and NPOR were set to zero. Using a well log interpretation software (Techlog® from Schlumberger), the reservoir porosity log was generated and added to the existing LAS (Log ASCCI Standard) files so that they could be loaded into CMG software. The spatial variation of porosity was generated and populated into the grid using Sequential Gaussian simulation[3] (Figure 2-4). The minimum and

---

[3] Sequential Gaussian simulation is a method that generates N number of data in a sequential way, satisfying covariance. Unlike the Kriging method, the sequential simulation preserves the mean, variance and distribution of the given data.

14

maximum cutoff values for porosity are 0.0 and 0.188 based on the minimum and maximum values of core-measured data (APPENDIX B: Porosity-permeability correlation).
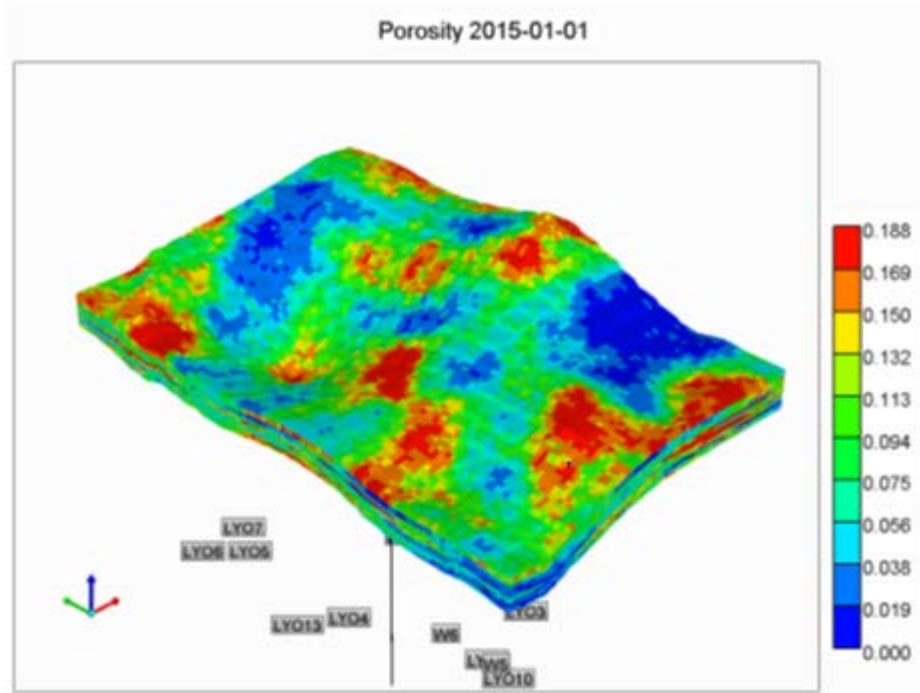
Figure 2-4. Porosity distribution over the entire area generated using Sequential Gaussian Simulation.

In an effort to build a realistic reservoir simulation model representative of the formation characteristics, core-measured data were used to develop a correlation between porosity and permeability. Permeability was estimated from three core-measured data of the Lyons formation, which original locations lie outside of the area of interests considered for the reservoir model, as indicated in Figure 2-5. These core data were obtained from the USGS Core Research Center. According to those measurements, the porosity-permeability correlations were developed to generate the permeability distributions in the geological reservoir model. The following general correlation equation was used,

$$k = a \times e^{b\phi} \tag{2.2}$$

where k is permeability, φ is porosity, and a and b are correlation parameters, obtained empirically based on core sample measurements.

15
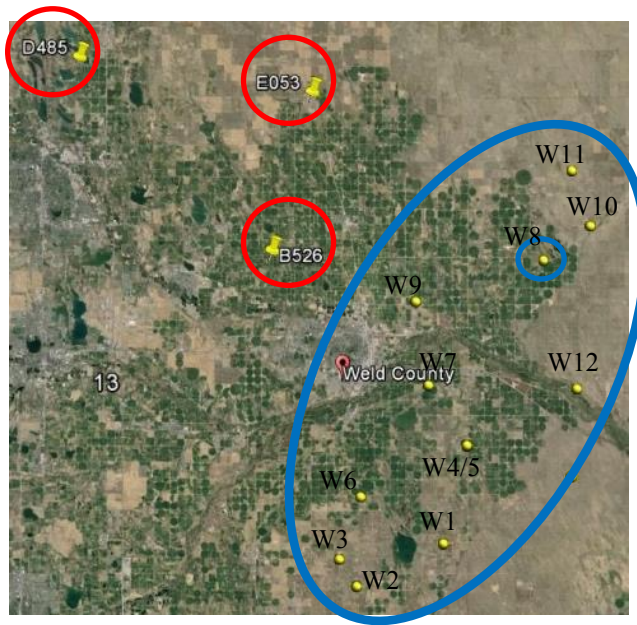
Figure 2-5. Locations of core data (D485, E053 and B526) adjacent to the target area.

Based on the core samples from the USGS Core Research Center (Table B 1, Table B 2 and Table B 3) in Appdendix B, there are three permeability-porosity correlations from different samples. Since permeability value is unknown in the target field, all three permeability estimates were considered independently in this research work. The permeability-porosity correlations are shown in Figure 2-6.
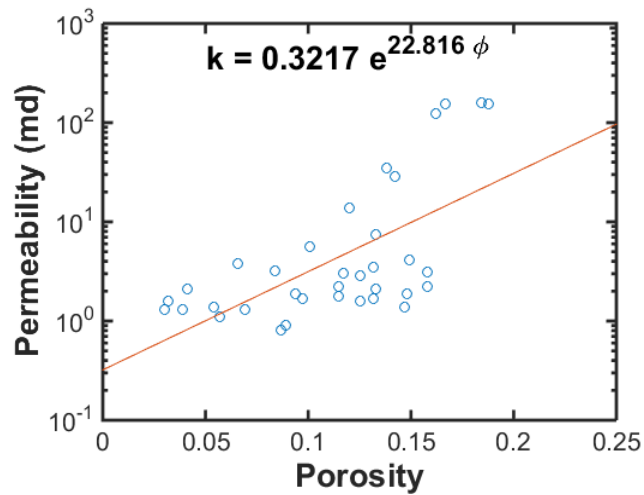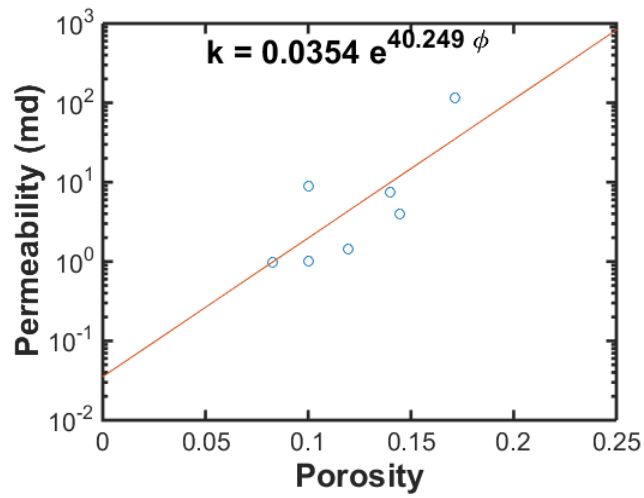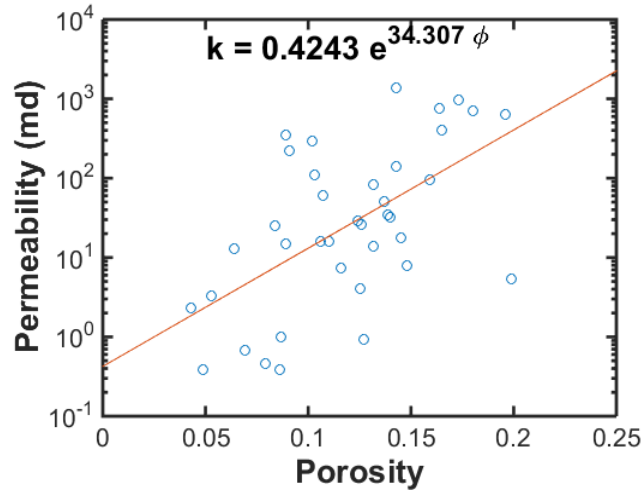
Figure 2-6. Permeability-Porosity correlation for different core samples D485, B526 and E053 accordingly.

17

There are three static reservoir models built based on different permeability-porosity correlations from samples E053, B526 and D485. These static reservoir models have maximum values of permeability as 299 md, 78 md and 25.2 md, respectively, so they are named low, intermediate and high permeability models. The permeability in horizontal directions, x and y, are assigned to be identical, and the permeability in the vertical direction, z, is set to be one tenth of the horizontal permeability, considering lower conductivity in the vertical direction. The porosity distribution of the reservoir model is shown in Figure 2-7. The permeability distributions for samples E053, B526 and D485 are shown in Figure 2-8. Permeability is an important factor in the production of sedimentary geothermal reservoirs, so preliminary simulations are performed in each permeability reservoir model, to determine the necessity of well enhancement techniques.
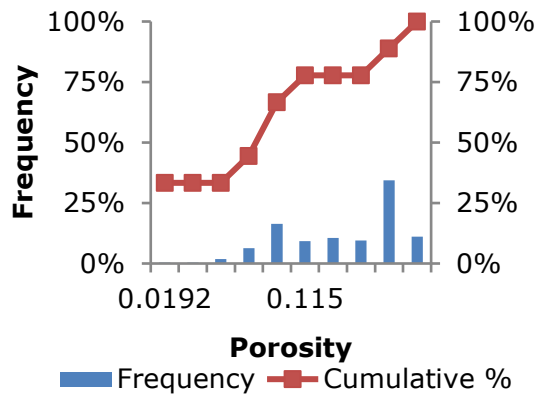
Figure 2-7. Histogram of porosity distribution of the reservoir model.

18
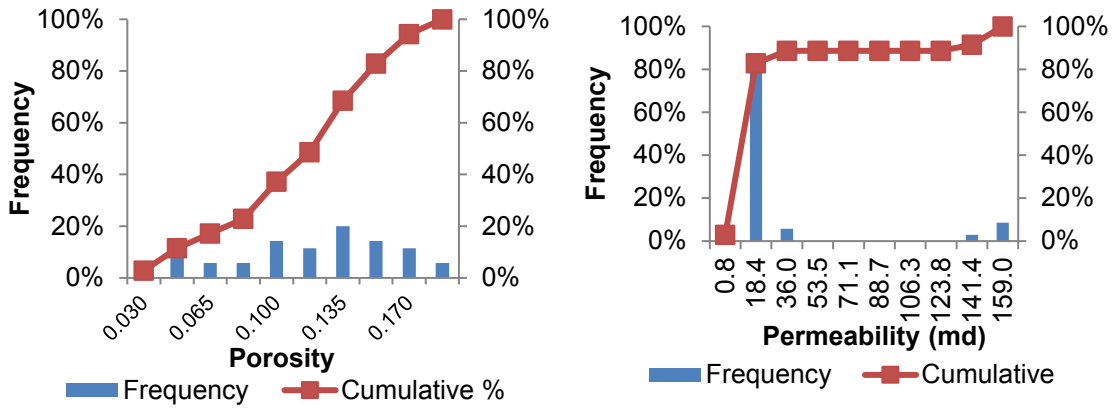
(a) Sample E053-Low
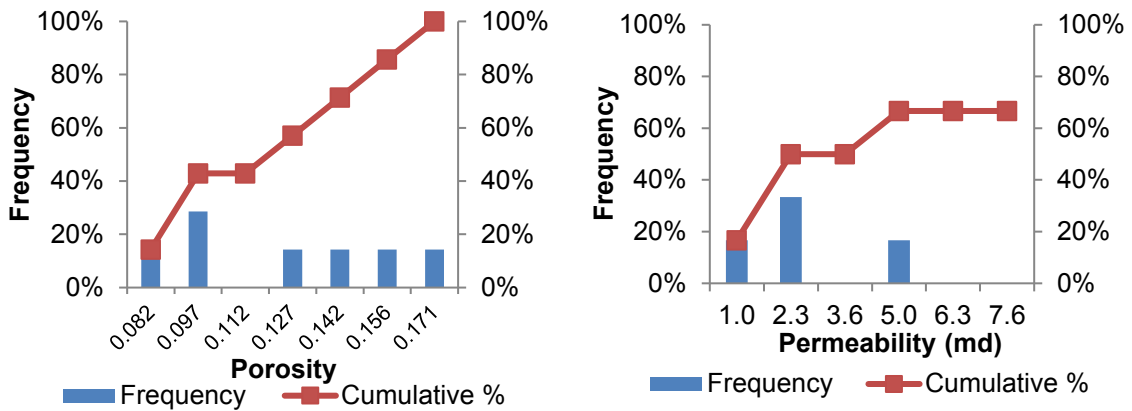
(b) Sample B526-Intermediate
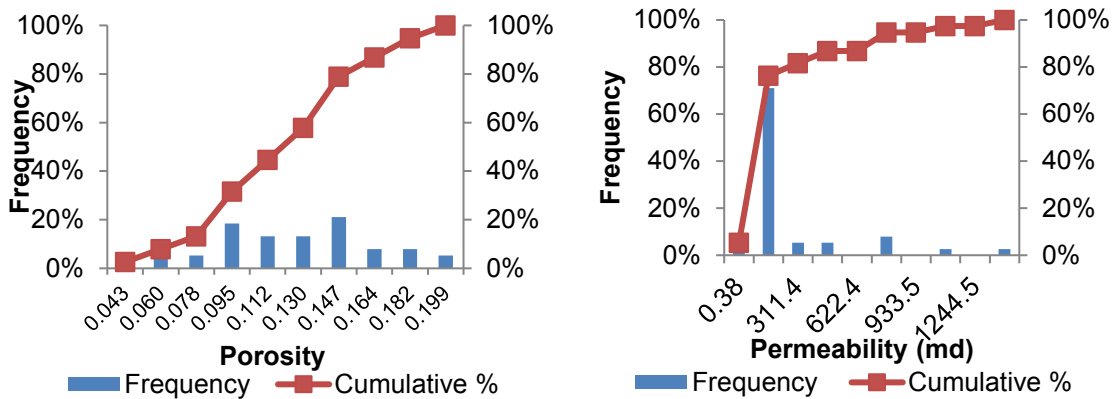
(c) Sample D485-High

Figure 2-8. Histogram of porosity and permeability distribution in the core measurements.

19

2.4   Building simulation model

Temperature values at every well location on each layer are calculated using the equation below.

$$Temp_{welllocation} = Temp_{surface} + TVD \times T_{grad}$$

(2.3)

The temperature distribution in the Lyons formation was estimated based on information from 12 water disposal wells, using the bottom-hole temperature data recorded in the well log header, and 23 production wells located in the Wattenberg field, but completed in different formations. The additional bottom-hole temperature data were obtained from Geothermal Prospector Map (https://maps.nrel.gov/geothermal-prospector/). The additional BHT data that do not reach the Lyons formation, were linearly extrapolated down to the Lyons formation. Assuming constant temperature gradients for the well locations, Kriging was used to generate the temperature distribution of each layer, and then these layer temperature distributions were stacked to create the 3D temperature distribution for the entire reservoir volume.

The porosity distribution in the Lyons formation was calculated by using a quadratic mean of density porosity and neutron porosity log values. Sequential Gaussian Simulation (SGS) was used for interpolation of porosity values between wells. Three core data sets with permeability measurements from the Lyons formation, obtained from the USGS Core Research Center, were used for the development of a porosity-permeability correlation. The permeability distribution was generated using this correlation, and the porosity distribution map from well locations. Figure 2-9 and Figure 2-10 show the temperature and porosity distribution for a selected layer of the Lyons formation.

Areas A (blue) and B (red) present the highest temperature areas, with temperature of 145 ˚C and 137 ˚C, respectively. However, the porosity in area A has a maximum value of 0.07, while that of area B is 0.178. Area B was selected due to its higher porosity (higher permeability) as the target area for the reservoir simulation study. At this point, the reservoir size is reduced from the original 28,000 m by 45,000 m to a submodel of 4,500 m by 4,500 m. Inside the submodel, temperature varies insignificantly, so the numerical reservoir model has a constant

20

temperature of 137 °C in the following simulations. This submodel is called the reservoir model in the following sections.

All other data including rock and fluid properties are listed in Table 3-1. A pair of wells is considered such that it can form a circulating geothermal doublet system. The default well distance is 1,500 m, the injection temperature is 80 °C, and both the injector and the producer operate at a constant target flow rate of 4,000 m^3/day. The wells are only perforated in the Lyons formation (layers 6 to 15 in the vertical direction, downward). Normal hydrostatic pressure gradient of 0.433 psi/ft was assumed for the initialization of reservoir pressures. The system is modeled as a single-phase system, containing only water.
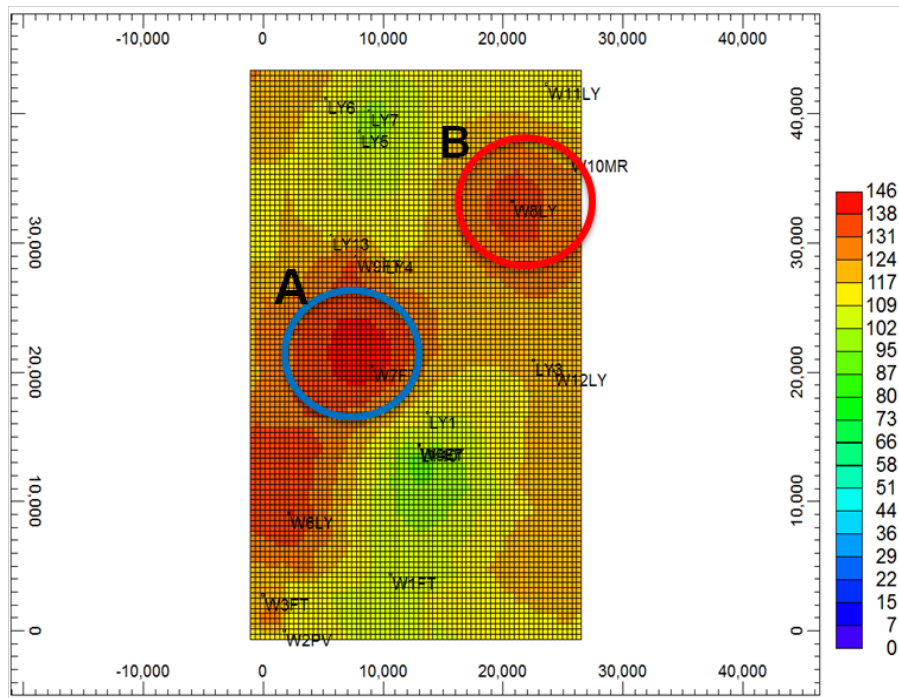
Figure 2-9. Temperature distribution for candidate area.

21

Figure 2-10. Porosity distribution for candidate area.

3   Reservoir Simulations

A commercial thermal reservoir simulator (STARS from Computer Modeling Group) was used in this work for the numerical reservoir modeling. The reservoir model was built using an orthogonal corner point grid with a resolution of 20×20×3.58 meters, with ten vertical layers. The areal grid size of 20×20 meters was verified to be small enough to have an acceptable approximation to the solution of an analytic model (Cho et al., 2015). It is assumed that horizontal permeability is equal in both horizontal directions (x and y) within each grid block, while the vertical permeability is one tenth of the horizontal permeability. A single aqueous phase is considered, with density and viscosity being a function of temperature, while the thermal properties of water are constant (i.e., heat capacity, thermal conductivity). Rock properties are assumed to be constant. Details of the properties are presented in the Appendix A.

This report is available at no cost from the National Renewable Energy Laboratory (NREL) at www.nrel.gov/publications.

Table 3-1. Parameters of numerical model of the sedimentary geothermal system.

Grid type	Orthogonal Corner Point
Normal grid size (m)	400 × 400
Refined grid size (m)	20 × 20
Refined gird area (km)	4.5 × 4.5
Porosity (fraction)	Geostatistics with log data
Permeability I&J (md)	Permeability model
Permeability K (md)	One tenth of Permeability I
Water viscosity (cp)	Internal Table
Water density (kg/m^3)	Internal Table
Volumetric Water heat capacity (kJ/m^3-K)	Internal Table
Water compressibility (1/kPa)	Internal Table
Water thermal conductivity	53,500
Rock compressibility (1/psi)	4.35×10^{-7}
Volumetric Rock Heat Capacity (J/m3-C)	2.38×10^6
Rock thermal conductivity (J/m-day-C)	1.496×10^5
Overburden/underburden heat loss	N/A
Reservoir Temperature (ºC)	Geostatistics with log data
Injection Temperature (ºC)	80
Well spacing (m)	1,500
Injection/production rate (m^3/day)	4,000
Minimum Timestep	30 days

The initial reservoir temperature is 137 °C and water injection temperature is 80 °C. In some geothermal systems, with EGS technology applied, the productivity can be improved to reach flow rate of 50–70 L/s (Moeck, 2014). The desired flow rate for injection and production wells is equal to 46 L/s (4000 m^3/day) in this research work. This is the maximum reachable flow rate in the base cases with horizontal wells with longitudinal fractures or transverse fractures. A maximum injection well bottomhole pressure of 35,300 kPa was used as a well constraint, to

23

maintain injection pressure below the typical fracture gradient of 0.60 psi/ft. The minimum production well bottomhole pressure was set to 21,300 kPa, to prevent the produced hot water from flashing into vapor at the wellhead. Details of the calculations of well pressure constraints are presented in Appendix B. The calculation of thermal breakthrough time is also described in Appendix B.

3.1   Preliminary Cases for Three Permeability Models

Other than the base case (Figure 3-1), vertical well doublet, simulation cases are categorized into four different models. Model A is a vertical well doublet system with hydraulic fractures. Model B is a horizontal well doublet system with open-hole completion. Model C is a horizontal well doublet system with longitudinal fractures. The last one, Model D is a horizontal well doublet system with multi-stage transverse fractures. One case from each model is used for the preliminary simulations for the choice of reservoir model permeability. Figure 3-2, Figure 3-3, Figure 3-4, and Figure 3-5 show the scheme of the four models.
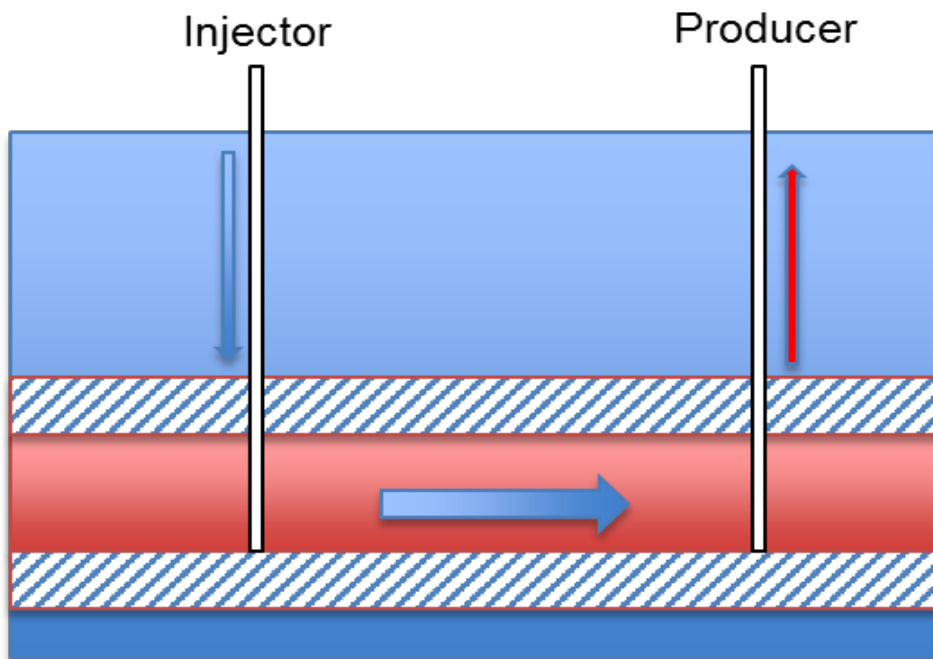
Figure 3-1. Vertical well doublet system (one injection well and one production well).

24
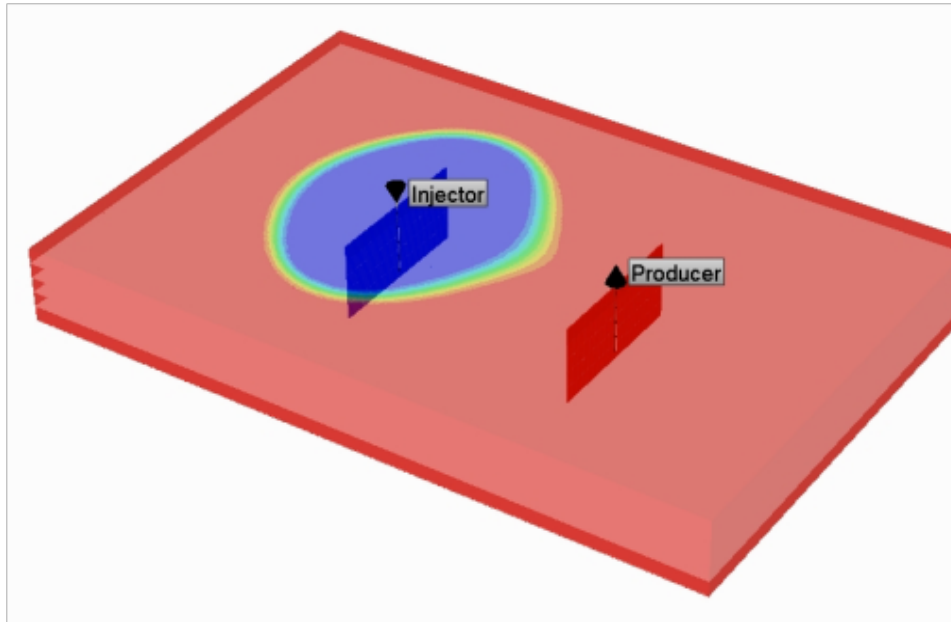
Figure 3-2. Model A (vertical well doublet system with hydraulic fractures).
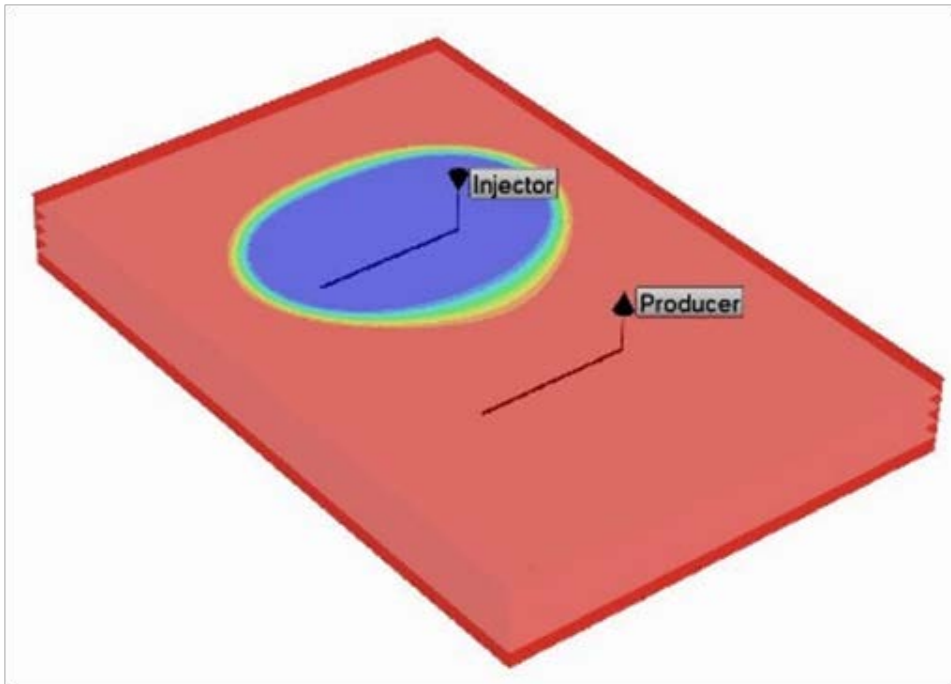
Figure 3-3. Model B (horizontal well doublet system with open-hole completion).

25
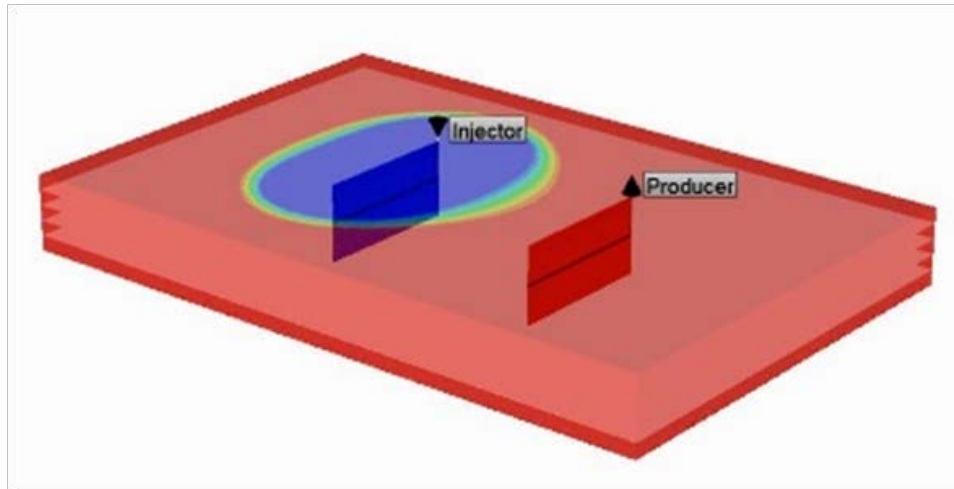
Figure 3-4. Model C (horizontal well doublet system with longitudinal fractures).
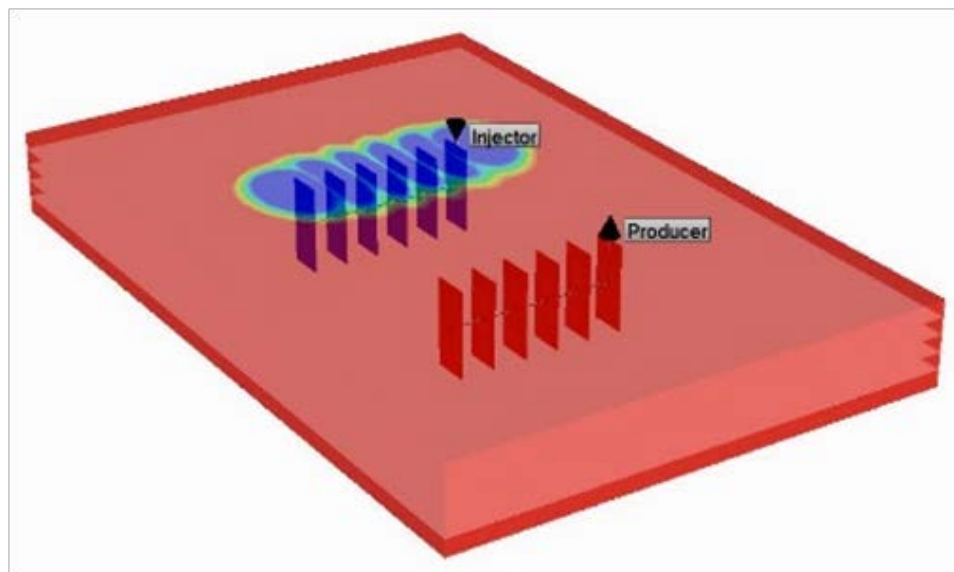
Figure 3-5. Model D (horizontal well doublet system with transverse fractures).

Table 3-2 shows the variable values for preliminary cases. Vertical well without fractures is the control case, as no well enhancement technique is used, named model O as the original. The following four cases are the base cases in models A, B, C, and D. They all use the default value for each variable if applicable. The definition and calculation of dimensionless fracture conductivity is described in Appendix D.

26

Table 3-2. Values of variable for preliminary cases in three different permeability cases

Model	Well configuration	Well spacing, D (m)	Length of horizontal section, L (m)	Dimensionless fracture conductivity, CfD	Fracture half-length, xf (m)	Fracture spacing, FS (m)
O	Vertical well without fractures	1500	-	-	-	-
A	Vertical well with fractures	1500	-	1.5	500	-
B	Horizontal well with open-hole completion	1500	1000	-	-	-
C	Horizontal well with longitudinal fractures	1500	1000	1.5	500	-
D	Horizontal well with multi-stage transverse fractures	1500	1000	1.5	500	200

3.1.1 Preliminary cases in low permeability reservoir model

Figure 3-6a shows the thermal breakthrough time for well doublet systems with vertical wells, vertical wells with fractures, horizontal wells with open-hole completion, horizontal wells with longitudinal fractures, and horizontal wells with five transverse fractures. Thermal breakthrough time is defined as the time required for the cold injected water to decrease the temperature of produced fluid below the initial reservoir temperature by one degree Celsius. For the low permeability reservoir model (Figure 3-6b), none of the preliminary cases can reach the target flow rate of 4000 m^3/day, while honoring the pressure restrictions in the injection and production wells. This will limit the generation of electricity from the geothermal energy production, below the desired requirement. Thermal breakthrough time is a function of the volume of reservoir affected by the flow and the rate of that flow. In this model, because of the limitation of permeability, the flow rate is limited, which limits the rate of extraction of thermal energy from the reservoir. The reservoirs appear to have long thermal breakthrough times (simulations are performed to 60 years; reservoir behaviors longer than that are not observed), but this is because of the limited flow rate and rate of thermal extraction[4]. Based on the hydraulic

---

[4] It is important to note throughout the report that when the target flow rate is not reached, the thermal breakthrough time is extended compared to cases where the target flow rate is reached, because the heat from the

behavior and thermal evolution, the application of reservoir enhancement techniques do not improve enough the performance of this low permeability geothermal system, since the target flow rate is not reached in any case. Figure 3-7 shows the productivity and injectivity index change in the process of time. It can be seen that the horizontal wells with fractures have an improved result compared to three other cases, but they are all below the value of 0.5 L/s-bar, which is not favorable in a geothermal reservoir.

(a)   (b)

Figure 3-6. Summary of thermal breakthrough time and change of production well flow rate as time changes for preliminary cases in low permeability reservoir model.

Figure 3-7. Change of productivity index and injectivity index as time changes for preliminary cases in low permeability reservoir model.

reservoir is not recovered as quickly. Cases in which the target flow rate is not reached cannot be compared to cases where the target flow rate is met. Other than observing that these cases are flow-limited, their results can generally be ignored.

28

3.1.2 Preliminary cases in intermediate permeability reservoir model

Figure 3-8a presents the thermal breakthrough time in different cases. Vertical wells and horizontal wells without fractures do not meet the target flow rate. They have thermal breakthrough times longer than 60 years and at 42 years, respectively, because of the poor hydraulic connection between the wells. Vertical wells with fractures, horizontal wells with longitudinal fractures, and horizontal wells with transverse fractures obtain breakthrough times of 32, 31 and 11 years, respectively. They are shorter than the values in the cases without fractures, because the existence of hydraulic fractures generates more surface area connecting the wells to the reservoir rock, which improves the system hydraulic behavior. In Figure 3-8b, it can be seen that in vertical wells, hydraulic fracturing help to improve the production flow rate, but not meeting the desired flow rate. In horizontal wells, hydraulic fracturing increase the production flow rate almost to the desired flow rate. In vertical and horizontal wells, well enhancement techniques decrease the thermal breakthrough time, because of the improved flow behavior in the reservoir. Figure 3-9 shows the productivity index and injectivity index change in the process of time. It can be seen that the horizontal wells with fractures have an improved result compared to three other cases, but they are all below the value of 0.5 L/s-bar, which is not favorable in a geothermal reservoir. To improve flow behavior and extend thermal evolution at the same time, further analysis is performed in section 3.2.

(a)   (b)

Figure 3-8. Summary of thermal breakthrough and change of production well flow rate as time changes for preliminary cases in intermediate permeability reservoir model.
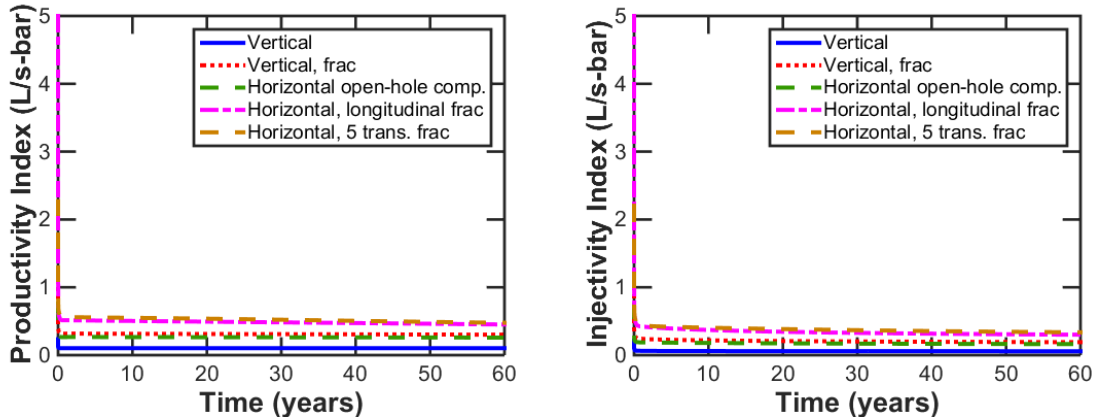
Figure 3-9. Change of productivity index and injectivity index as time changes for preliminary cases in ilow permeability reservoir model.

3.1.3 Preliminary cases in high permeability reservoir model

For preliminary cases in high permeability reservoir model in Figure 3-10, other than vertical wells without fractures, all other well configurations reach the desired flow rate throughout time and they reach thermal breakthrough at similar times. This indicates that drilling horizontal wells would provide good enough flow behavior for a geothermal reservoir with a high permeability. And the application of hydraulic fracturing improves slightly on the thermal breakthrough time of the reservoir. Figure 3-10 shows the productivity and injectivity index for preliminary cases in the high permeability model, and they have the same trend as in low and intermediate permeability models, while the values can be as high as 1.2 L/s-bar. However, in the high permeability static reservoir model, it is not necessary to apply well enhancement techniques. Although well enhancement techniques have a large impact on PI, especially compared to vertical well doublet, they do not change thermal breakthrough time much, which is the main criterion to select the proper well configuration.
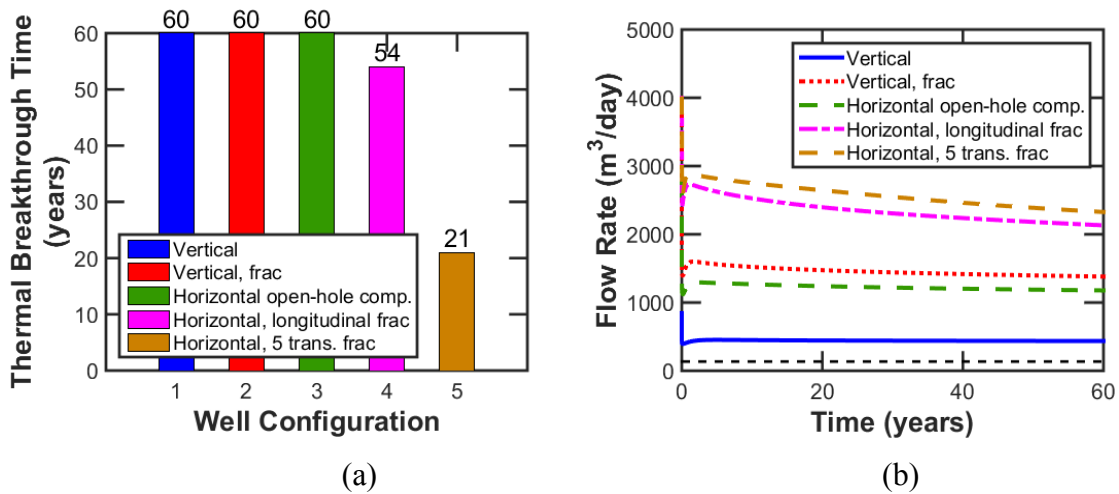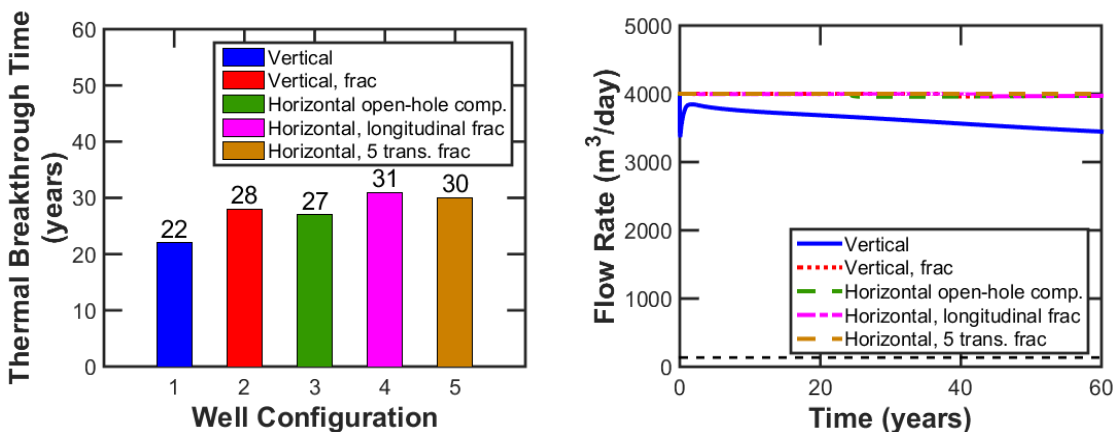

Figure 3-10. Summary of thermal breakthrough time and change of production well flowrate as time changes for preliminary cases in high permeability reservoir model.
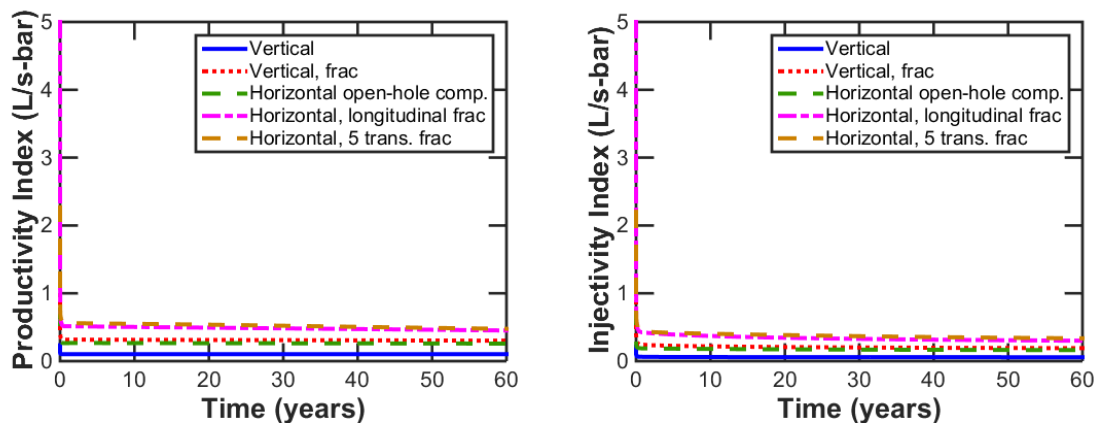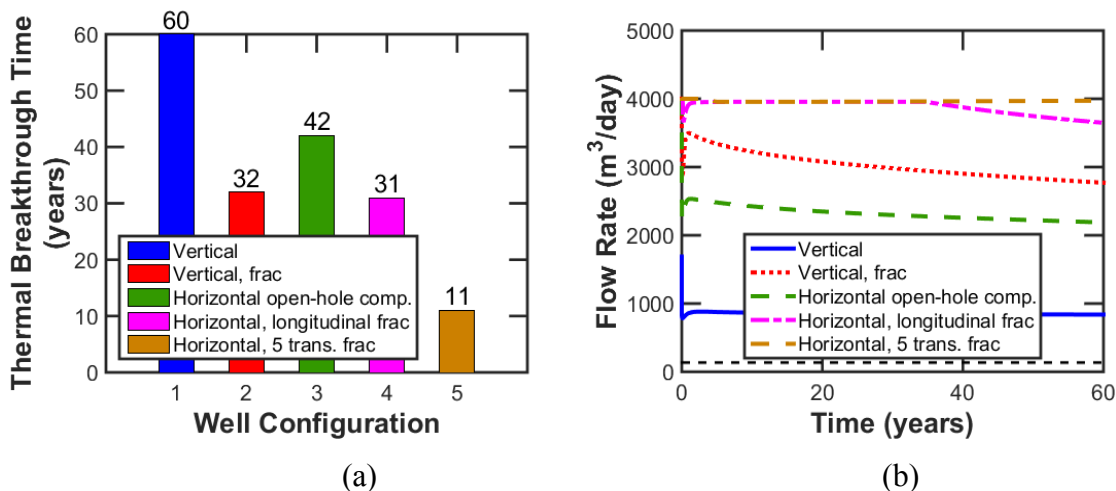
30
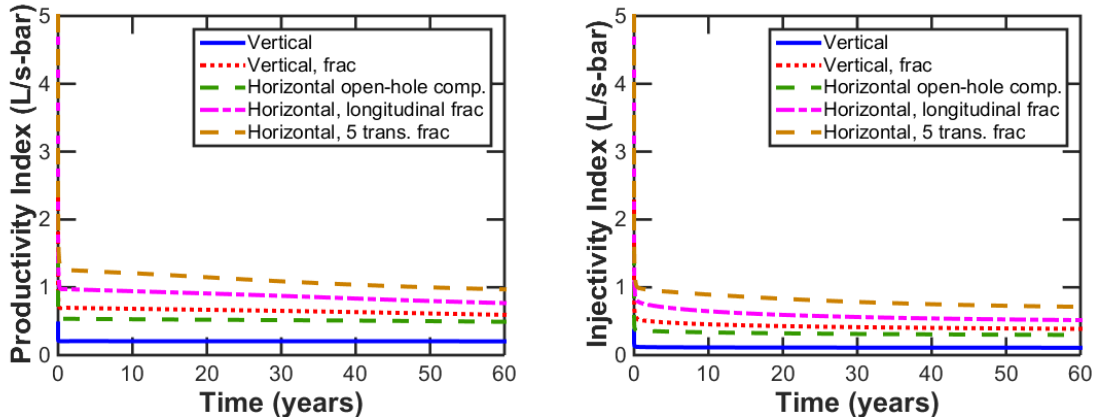
Figure 3-11. Change of productivity index and injectivity index as time changes for preliminary cases in intermediate permeability reservoir model.

3.2 Additional Simulation Cases for Intermediate Permeability Model

The intermediate permeability reservoir model was selected for further analysis on the effects of length of horizontal section, fracture spacing and fracture half-length on the reservoir performance.

3.2.1 Effect of horizontal section length on horizontal wells with open-hole completion (model B)

Figure 3-12 shows that longer horizontal section length is more favorable for well productivity, because increasing horizontal length increases flow rates, as shown in Figure 3-13. In horizontal wells with open-hole completion, with the same well spacing, a longer horizontal section length creates a larger sweeping area for the flow, thus enhancing the flow rate and sequentially productivity index, as shown in Figure 3-14. Thermal breakthrough time is a result affected by flow rate, sweeping volume and reservoir porosity. Figure 3-14(a), (b) and (c) have different flow rates, sweeping areas, and porosity distribution of its sweeping volume, so the differences in calculated thermal breakthrough time cannot be explained solely by the different values of length of horizontal section. However, it indicates that the length of horizontal section would affect the thermal evolution in a reservoir system with horizontal wells, which will be investigated further in models C and D in the following sections.

31
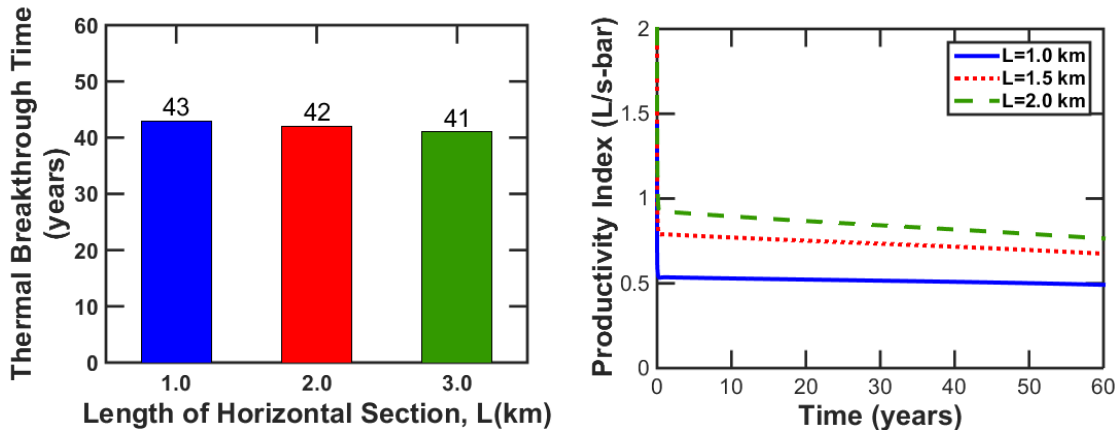
Figure 3-12. Summary of thermal breakthrough time and change of productivity index in the process of time for horizontal wells with open-hole completion cases with different horizontal section length values.
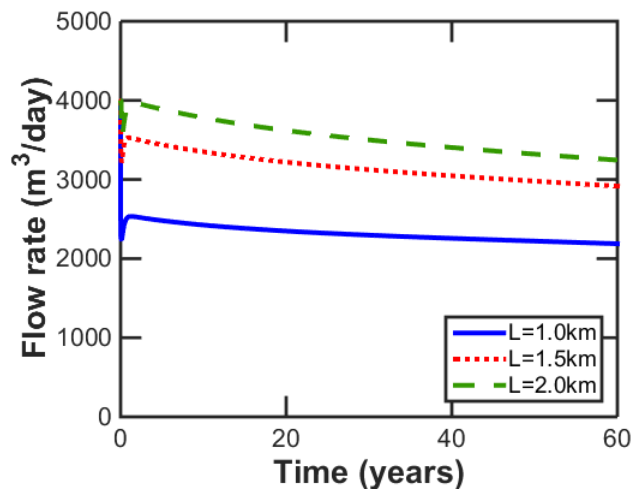
Figure 3-13. Change of flow rate in the process of time for horizontal wells with open-hole completion cases with different horizontal section length values.

32
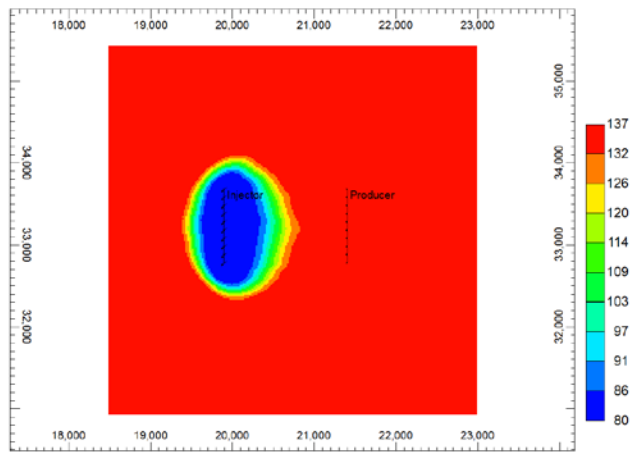
(a)
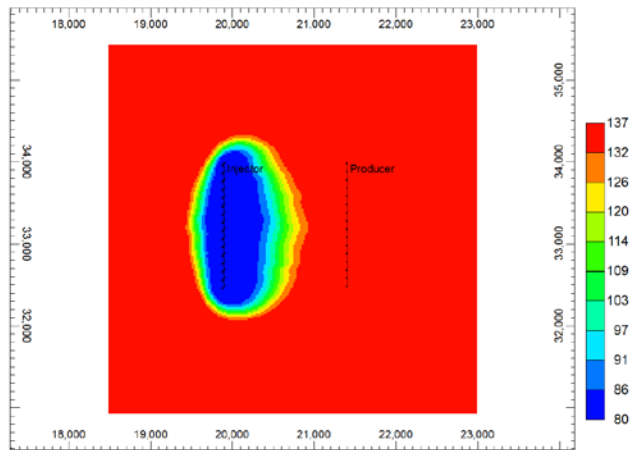
(b)
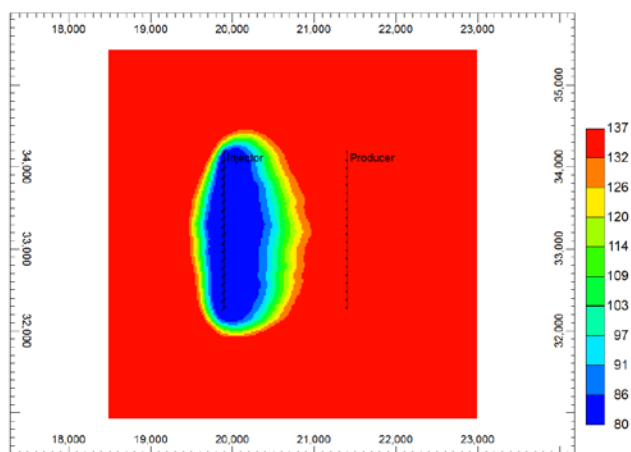
(c)

Figure 3-14. Aerial view temperature distribution after 30 years of production for horizontal wells with open-hole completion, with horizontal section lengths: 1.0 km (a), 1.5 km (b), and 2.0 km (c).

33

3.2.2 Effect of horizontal sections lengths on horizontal wells with longitudinal fractures (model C)

Figure 3-15 shows that a longer horizontal section length provides a longer thermal breakthrough, and increase the productivity index. With longitudinal fractures, the fluid is distributed through the fracture with help of the well horizontal section, and a larger reservoir volume with linear flow between the two fracture planes is developed. Since a larger reservoir volume is being flooded with cold water at the same target flow rate, the thermal breakthrough time is longer for longer horizontal wells. With the same flow rate, the case with a longer lateral length provides a higher PI/II value.
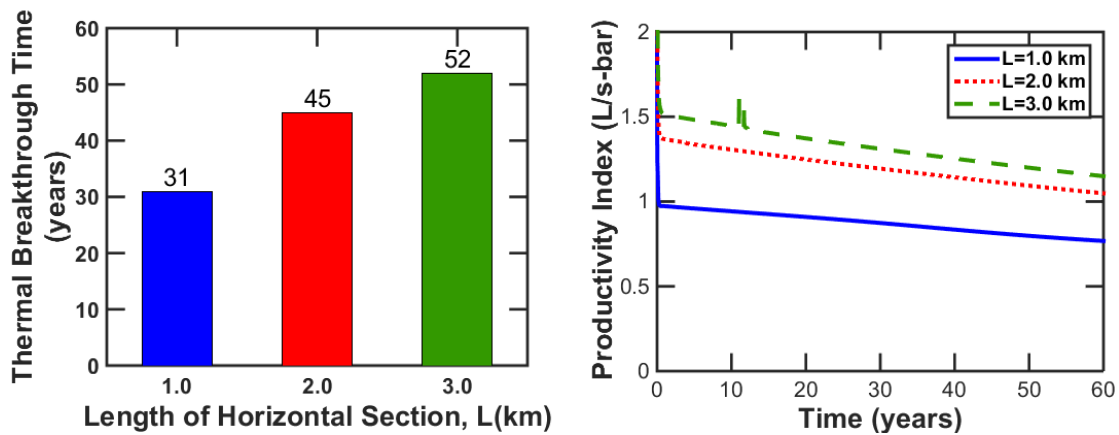
Figure 3-15. Summary of thermal breakthrough time and change of productivity index in the process of time for horizontal well with longitudinal fractures cases with different horizontal section length values.
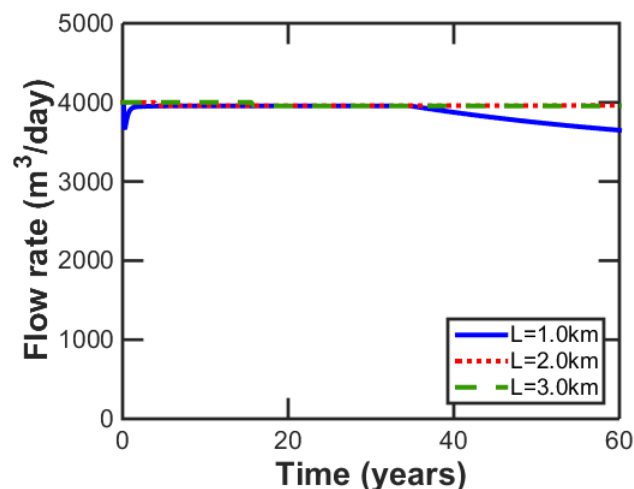
Figure 3-16. Change of flow rate in the process of time for horizontal well with longitudinal fractures cases with different horizontal section length values.

34

3.2.3 Effect of fracture spacing in horizontal wells with transverse fractures (model D)

Figure 3-17 shows the schematic diagrams for cases in model D with different values of fracture spacing. A fracture spacing of zero means that there is only one transverse fracture in that case, since there is no other fractures to calculate the fracture spacing. As can be seen in Figure 3-18, the case with a single transverse fracture case has a low PI value, and does not meet the target flow rate. An increased number of transverse fractures increases the PI, but decreases the thermal breakthrough time. The cases with 5 and 10 transverse hydraulic fractures meet the target flow rate (Figure 3-19).

(a)

(b)

35
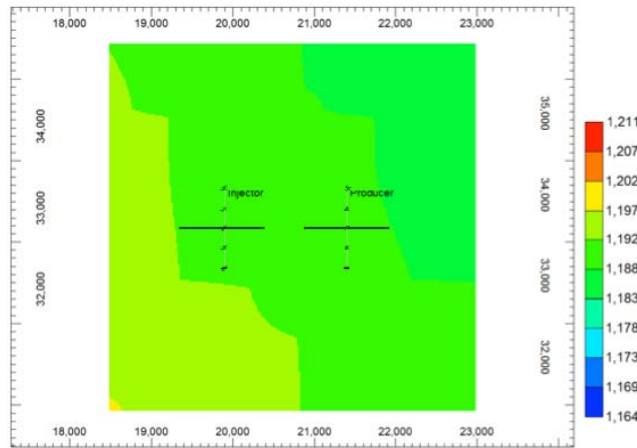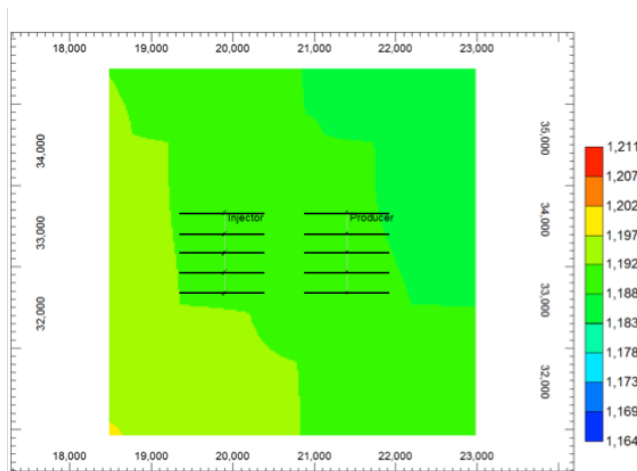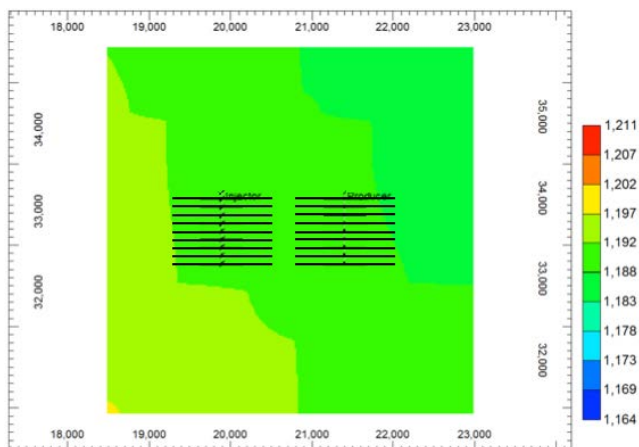
(c)

Figure 3-17. Schematic diagram of well configurations in horizontal well doublet system with transverse fractures with different values of fracture spacing: 0 km (1 fracture) (a), 200 m (b), and 100 m (c).
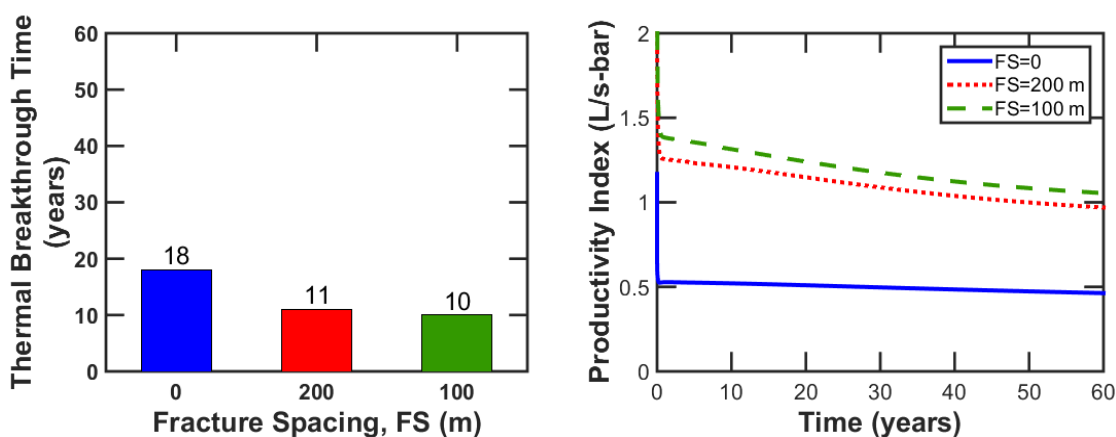
Figure 3-18. Summary of thermal breakthrough and change of productivity index in the process of time for horizontal well with transverse fracture cases with different fracture spacing values.
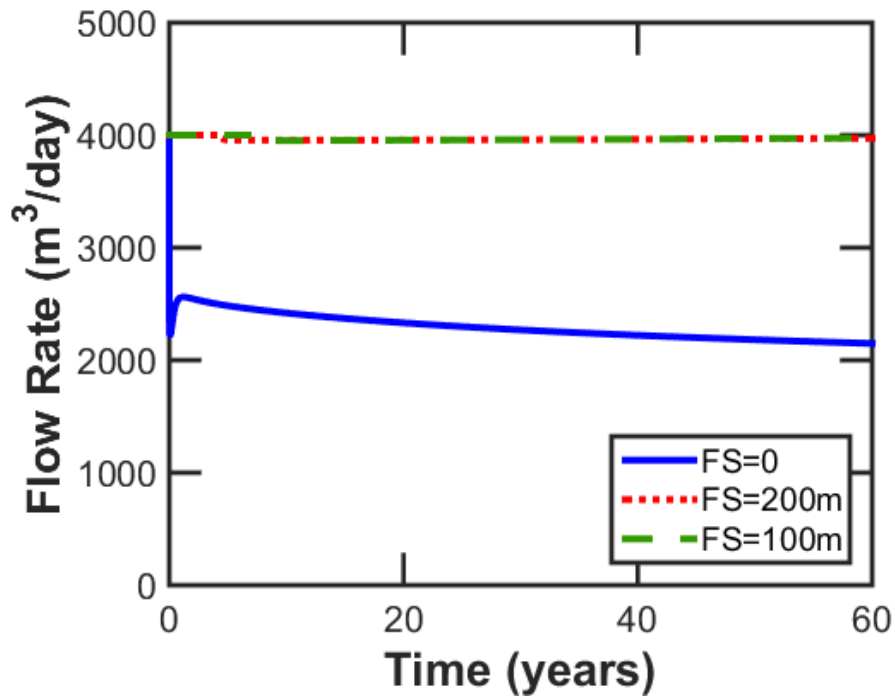
Figure 3-19. Change of production well flow rate as time changes for horizontal well with transverse fracture cases with different fracture spacing values.

3.2.4 Effect of fracture spacing and fracture half-length on horizontal wells with transverse fractures (model D)

In model D, fracture half-length and fracture spacing have an impact on the reservoir thermal evolution and hydraulic behavior. In order to see the effect of these two variables, another simulation case, was run. This new case has fracture spacing of 100 m and fracture half-length of 250 m, which shares the same fracture area as the old case (fracture spacing of 200 m and fracture half-length of 500 m). Figure 3-20 shows the schematic diagrams for cases in model D with different values of fracture spacing and fracture half-length.

37
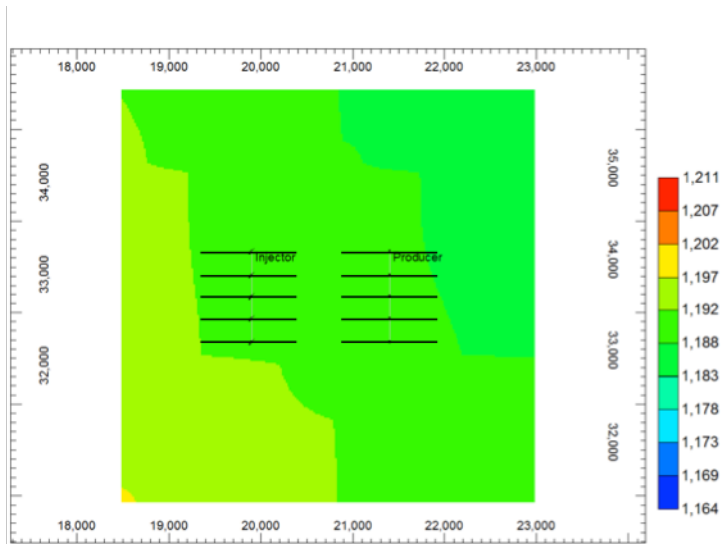
(a)
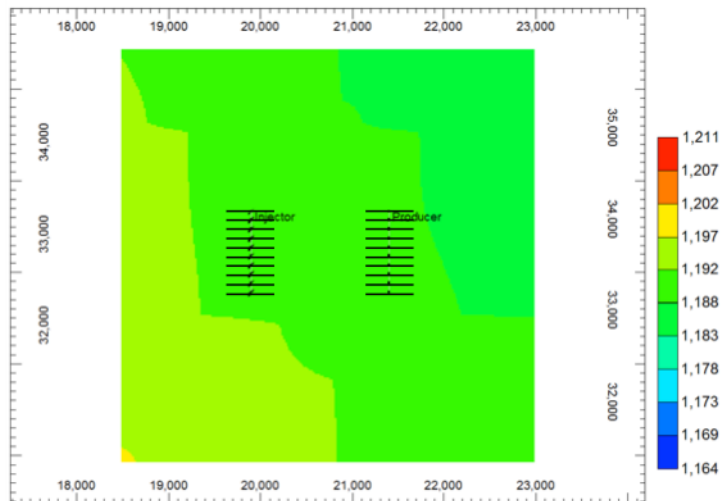
(b)

Figure 3-20. Schematic diagram of well configurations in horizontal well doublet system with transverse fractures with different values of fracture spacing and fracture half-length: 200 km and 500 m (a), 100 m and 250 m (b).

Figure 3-21a shows that the thermal breakthrough time from old case to new case increases from 11 years to 21 years. The new case, which has a shorter fracture half-length, has a longer spacing between the injection and production wells, thus increasing the thermal breakthrough time. Figure 3-21b shows that the productivity index decreases about 10 % in the new case. However, the decrease in productivity index is acceptable, considering the increase in thermal breakthrough time.

38
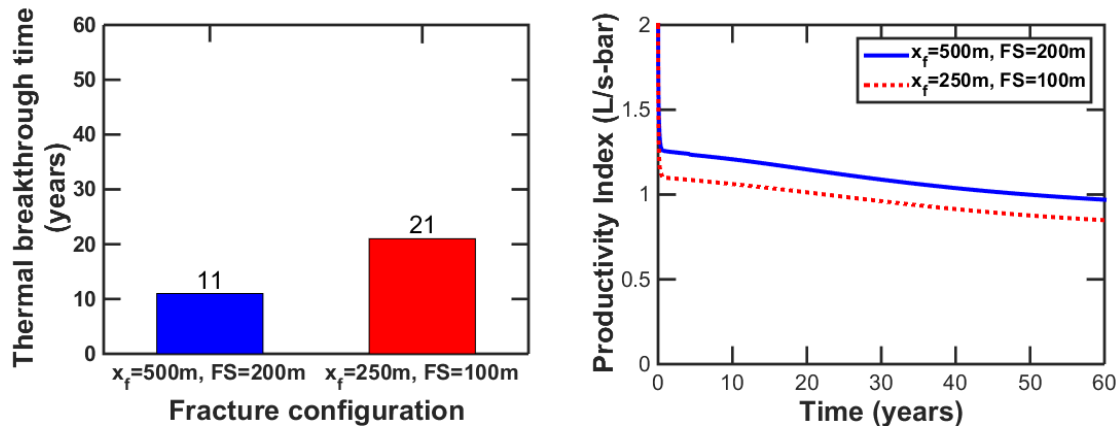
Figure 3-21. Summary of thermal breakthrough and change of productivity index in the process of time horizontal well with transverse fracture cases with same fracture surface area

3.3   Summary

This section presented an overview of the significance of different variables in the design of hydraulic fractures in a geothermal reservoir. An estimation of the permeability in the reservoir is the key component to decide if well enhancement techniques are necessary or not. For a reservoir with too low permeability, if a desired flow rate cannot be reached, more advanced enhancement techniques are required. For a reservoir with high enough permeability, the application of hydraulic fracturing does not improve the system performance significantly, so it is not economical for the production.

A reservoir with intermediate permeability (ranges from 7.81 md to 78 md in this research work) is a proper candidate to apply reservoir enhancement techniques, such as, horizontal wells and hydraulic fracturing. Usually, vertical wells with or without fractures, and horizontal wells with open-hole completion cannot provide desired flow rate. Horizontal wells with fractures are advantageous for the hydraulic behavior and thermal evolution of the system. In limited space, a horizontal well doublet system with a long lateral section and short well spacing is preferred for both longitudinal and transverse fracture cases. In addition, in the cases of transverse fractures, shorter fracture spacing contributes more fractures, thus facilitating the hydraulic behavior. In a certain area of interest, both horizontal wells with longitudinal fractures and horizontal wells with transverse fractures facilitate the thermal recovery in a geothermal reservoir. While the former improves more on thermal breakthrough time, the latter enhances more on the hydraulic behavior.

39

4 Conclusions and Suggestions

This report represents the necessity and advantage of the application of well enhancement techniques (i.e., hydraulic fracturing) to the production in a sedimentary geothermal reservoir. Horizontal wells with longitudinal or transverse fractures are beneficial because of their improvement on flow behavior and thermal evolution.

Permeability acts as the key component in the production of a sedimentary geothermal reservoir. In this research work, the low permeability model has permeability ranges from 2.81 md to 25.2 md. The intermediate permeability model has a permeability range from 7.81 md to 78 md, and the high permeability model has permeability values ranging from 30.3 md to 299 md. Well enhancement techniques may not be sufficient to make it a commercial geothermal electricity generation project in the low permeability reservoir. Reservoirs with high enough permeability may not need the optimization process of well configuration in order to meet the desired flow rate for electricity generation, like in the case with high permeability in this study. Geothermal reservoirs with intermediate permeability values could be a good candidate formation to apply hydraulic fracturing techniques and optimization of well configurations.

Hydraulic fracturing techniques improve the production in both vertical wells and horizontal wells. Horizontal wells with fractures have a more beneficial performance compared to vertical wells with fractures. Thus horizontals wells with longitudinal fractures or multi-stage transverse fractures provide good improvement on production.

References

Cho, J., Augustine, C. and Zerpa, L.E., 2015. Validation of a Numerical Reservoir Model of Sedimentary Geothermal Systems Using Analytical Models, Stanford Geothermal Workshop, Stanford, CA.

Gringarten, A.C. and Sauty, J.P., 1975. A theoretical study of heat extraction from aquifers with uniform regional flow. Journal of Geophysical Research, 80(35): 4956-4962.

GTO-DOE, 2012. Geothermal Electricity Technology Evaluation Model (GETEM). In: G.T. Office (Editor). US Department of Energy.

Higley, D.K. and Cox, D.O., 2007. Oil and gas exploration and development along the Front Range in the Denver Basin of Colorado, Nebraska, and Wyoming. Petroleum Systems and Assessment of Undiscovered Oil and Gas in the Denver Basin Province, Colorado, Kansas, Nebraska, South Dakota, and Wyoming—USGS Province, 39.

Matuszczak, R., 1973. Wattenberg Field, Denver Basin, Colorado. The Mountain Geologist, 10(3): 99-107.

Moeck, I.S., 2014. Catalog of geothermal play types based on geologic controls. Renewable and Sustainable Energy Reviews, 37: 867-882.

Morgan, P., Sares, M. and Dechesne, M., 2009. Stratigraphic Control of Temperatures in the Wattenberg Field, Denver Basin, Colorado, AAPG Annual Convention, Denver, Colorado.

APPENDIX A: Well log analysis

Table A 1. Summary of well information availability of the 12 water disposal wells.

#	UWID	Lyons Top (ft)	Lyons Bottom(ft)	GR	DPOR	NPOR	Resistivity
1	05-123-30367	8104	8144	x	x		x
2	05-123-26004	8372	8420	x	x	x	x
3	05-123-29168	8544	8940	x	x	x	x
4	05-123-16804	7963	8639	x			
5	05-123-29536	7976	8050	x			x
6	05-123-19688	8191	8472	x	x	x	x
7	05-123-27116	8642	8696	x	x	x	x
8	05-123-25694	7824	8528	x	x	x	x
9	05-123-35841	7234	9050	x	x	x	x
10	05-123-32207	7202	8508	x	x	x	x
11	05-123-15685	7752	8630	x	x	x	x
12	05-123-23332	7163	7313	x	x	x	x

APPENDIX B: Porosity-permeability correlation – B526, D485 and E053

Table B 1. Core measurement data: E053

Sample Depth (ft)	Porosity (v/v)	Permeability (mD)
9174.5	0.167	155.0
9175.5	0.162	125.0
9176.5	0.120	14.0
9177.5	0.119	-
9178.5	0.089	0.9
9179.5	0.082	-
9180.5	0.054	1.4
9181.5	0.069	1.3
9182.5	0.142	29.0
9183.5	0.133	7.5
9184.5	0.101	5.7
9185.5	0.041	2.1
9186.5	0.050	-
9187.5	0.032	1.6
9188.5	0.039	1.3
9189.5	0.048	0.0
9190.5	0.059	0.0
9191.5	0.057	0.0
9192.5	0.063	0.0
9193.5	0.054	0.0
9194.5	0.066	3.8
9195.5	0.057	1.1
9196.5	0.093	0.0
9197.5	0.096	0.0
9198.5	0.133	2.1
9199.5	0.149	4.1
9200.5	0.132	1.7
9201.5	0.115	2.2

43

Sample Depth (ft)	Porosity (v/v)	Permeability (mD)
9202.5	0.126	0.0
9203.5	0.158	3.1
9204.5	0.138	35.0
9205.5	0.184	159.0
9206.5	0.188	156.0
9207.5	0.132	3.5
9208.5	0.125	2.9
9209.5	0.158	2.2
9210.5	0.084	3.2
9211.5	0.147	1.4
9212.5	0.109	-
9213.5	0.110	0.0
9214.5	0.111	0.0
9215.5	0.094	1.9
9216.5	0.115	1.8
9217.5	0.148	1.9
9218.5	0.097	1.7
9219.5	0.125	1.6
9220.5	0.117	3.0
9221.5	0.062	0.0
9222.5	0.087	0.8
9223.5	0.072	-
9224.5	0.039	-
9225.5	0.063	0.0
9226.5	0.030	1.3
9227.5	0.060	0.0
9228.5	0.073	0.0
9229.5	0.063	0.0
9231.5	0.085	0.0
9232.5	0.033	0.0
9233.5	0.066	0.0

Table B 2. Core measurement data: B526

Sample Depth (ft)	Porosity (v/v)	Permeability (mD)
9026.10	0.0964	8.91
9040.40	0.1713	116.
9046.00	0.0824	0.991
9056.20	0.1399	7.60
9060.80	0.1445	3.93
9062.30	0.1195	1.42
9069.00	0.093	1.03

Table B 3. Core measurement data: D485

Sample Depth (ft)	Porosity (v/v)	Permeability (mD)
6123.0	0.082	-
6124.0	0.180	695.0
6125.0	0.143	1400.0
6126.0	0.188	-
6127.0	0.173	975.0
6128.0	0.124	29.0
6129.0	0.086	0.4
6130.0	0.087	1.0
6131.0	0.069	0.7
6132.0	0.043	2.3
6133.0	0.125	4.1
6134.0	0.049	0.4
6135.0	0.079	0.5
6136.0	0.148	7.9
6137.0	0.159	97.0
6138.0	0.165	404.0
6139.0	0.164	760.0
6140.0	0.089	352.0

Sample Depth (ft)	Porosity (v/v)	Permeability (mD)
6141.0	0.132	83.0
6142.0	0.145	18.0
6143.0	0.084	25.0
6144.0	0.102	293.0
6145.0	0.139	35.0
6146.0	0.103	110.0
6147.0	0.140	32.0
6148.0	0.091	221.0
6149.0	0.064	13.0
6150.0	0.053	3.3
6151.0	0.110	16.0
6152.0	0.116	7.4
6153.0	0.107	61.0
6154.0	0.126	26.0
6155.0	0.089	15.0
6156.0	0.132	14.0
6157.0	0.137	51.0
6158.0	0.199	5.4
6159.0	0.196	630.0
6160.0	0.106	16.0
6161.0	0.143	142.0
6162.0	0.127	0.9
6163.0	0.043	-

APPENDIX C: Temperature data

Table C 1. Temperature data in the Niobrara.

#	Well API	Depth of measurement	Measured Temperature	Corrected Temperature	T_{surf}	Geothermal Gradient	GL	Average gradient
		(m)	(˚C)	(˚C)	(˚C)	(˚C/km)	(m)	(˚C/km)
NBR1	05-123-10976-0000	2,222.9	82.2	88.0	12.7	33.8	1,426.2	
NBR2	05-123-11185-0000	2,170.8	77.2	82.9	12.7	32.3	1,427.7	
NBR3	05-123-11840-0000	2,119.0	83.3	88.8	12.7	35.9	1,409.4	
NBR4	05-049-05000-2962	2,189.7	88.9	94.6	12.6	37.4	1,454.2	
NBR5	05-123-12888-0000	2,181.5	85.0	90.7	12.6	35.7	1,431.6	
NBR6	05-049-05000-3650	2,109.2	93.9	99.4	12.7	41.1	1,411.8	38.5
NBR7	05-123-15084-0000	2,248.2	92.2	98.0	12.6	38.0	1,450.5	
NBR8	05-123-16053-0000	2,211.9	91.7	97.4	12.6	38.3	1,448.7	
NBR11	05-049-05000-4208	2,422.6	90.0	95.3	12.7	40.7	1,423.7	
NBR12	05-123-19010-0000	2,215.9	102.8	108.5	12.7	43.2	1,432.3	
NBR13	05-123-20130-0000	2,130.9	89.4	95.0	12.8	38.5	1,406.7	
NBR14	05-123-24078-0000	2,238.5	112.8	118.6	12.6	47.3	1,465.2	

Table C 2. Temperature data in the Dakota J sand.

#	Well API	Depth of measurement	Measured Temperature	Corrected Temperature	T_{surf}	Geothermal Gradient	GL	Average gradient
		(m)	(˚C)	(˚C)	(˚C)	(˚C/km)	(m)	(˚C/km)
DJS1	05-123-23002-0000	2326.2	102.8	108.8	12.6	41.3	1468.5	
DJS2	05-123-23265-0000	2204.6	95.0	100.7	12.8	39.8	1403.9	
DJS4	05-123-23766-0000	2356.1	104.4	110.5	12.5	41.6	1478.3	
DJS5	05-123-23771-0000	2390.9	106.7	112.8	12.7	41.9	1443.2	
DJS7	05-123-24131-0000	2233.3	103.9	109.7	12.7	43.4	1427.7	
DJS8	05-123-24227-0000	2223.2	95.0	100.8	12.7	39.6	1424.3	
DJS10	05-123-24641-0000	2254.0	93.9	99.7	12.6	38.6	1441.7	
DJS11	05-123-24643-0000	2254.9	103.3	109.2	12.6	42.8	1444.8	41.2
DJS12	05-123-24717-0000	2361.6	101.7	107.8	12.4	40.4	1469.1	
DJS13	05-123-26200-0000	2446.6	108.9	115.2	12.3	42.0	1528.6	
DJS14	05-123-26366-0000	2056.2	93.9	99.2	12.7	42.0	1418.5	
DJS15	05-123-26616-0000	2395.4	104.4	110.6	12.7	40.9	1440.5	
DJS17	05-123-27352-0000	2212.8	96.1	101.8	12.7	40.2	1414.6	
DJS18	05-123-27394-0000	2413.1	107.2	113.5	12.6	41.8	1460.0	

Table C 3. 25 temperature data in the Morrison.

#	Well API	Depth of measurement	Measured Temperature	Corrected Temperature	T_{surf}	Geothermal Gradient	GL	Average gradient
		(m)	(˚C)	(˚C)	(˚C)	(˚C/km)	(m)	(˚C/km)
MRS1	05-123-10033-0000	2252.2	83.3	89.2	12.9	33.8	1383.8	
MRS2	05-049-05000-3869	2409.7	110.0	116.2	12.6	43.0	1464.6	
MRS3	05-049-05000-3950	2423.2	107.2	113.5	12.5	41.6	1474.6	
MRS4	05-123-16246-0000	2426.2	105.0	111.3	12.6	40.6	1465.5	
MRS5	05-049-05000-3967	2450.6	104.4	110.8	12.5	40.1	1476.5	
MRS6	05-123-16264-0000	2467.4	105.6	111.9	12.4	40.3	1492.3	
MRS8	05-123-16298-0000	2413.4	100.0	106.2	12.7	38.7	1448.4	
MRS10	05-049-05000-3997	2414.0	107.8	114.0	12.6	42.0	1467.3	
MRS11	05-123-16431-0000	2417.7	109.4	115.7	12.6	42.6	1467.9	40
MRS12	05-123-16519-0000	2460.7	101.1	107.5	12.5	38.6	1492.9	
MRS13	05-123-17330-0001	2405.2	113.3	119.6	12.5	44.5	1491.7	
MRS14	05-049-05000-4371	2432.3	101.7	108.0	12.6	39.2	1467.3	
MRS15	05-123-20086-0000	2250.0	95.0	100.8	12.8	39.1	1389.3	
MRS16	05-123-20543-0000	2236.3	98.9	104.7	12.8	41.0	1387.1	
MRS17	05-123-20572-0000	2248.5	101.1	106.9	12.8	41.8	1391.7	
MRS18	05-123-20581-0000	2227.8	97.2	103.0	12.9	40.4	1385.0	

#	Well API	Depth of measurement	Measured Temperature	Corrected Temperature	T_{surf}	Geothermal Gradient	GL	Average gradient
		(m)	(˚C)	(˚C)	(˚C)	(˚C/km)	(m)	(˚C/km)
MRS19	05-123-20656-0000	2238.5	96.7	102.5	12.9	40.0	1384.7	
MRS20	05-123-21882-0000	2245.2	95.6	101.4	12.8	39.4	1386.5	
MRS21	05-123-21968-0000	2269.8	97.2	103.1	12.8	39.8	1394.5	
MRS22	05-123-22021-0000	2238.5	97.8	103.6	12.8	40.5	1392.6	
MRS23	05-123-22062-0000	2258.0	97.8	103.6	12.8	40.2	1393.2	
MRS24	05-123-22064-0000	2259.5	99.4	105.3	12.8	40.9	1393.5	
MRS25	05-123-22260-0000	2270.8	96.7	102.5	12.8	39.5	1386.8	
MRS28	05-123-26005-0000	2269.5	99.4	105.3	12.7	40.8	1424.0	
MRS29	05-123-26038-0000	2323.5	100.0	106.0	12.5	40.2	1462.7	

Table C 4. 25 temperature data in the Lakota.

#	Well API	Depth of measurement	Measured Temperature	Corrected Temperature	T_{surf}	Geothermal Gradient	GL	Average gradient
		(m)	(˚C)	(˚C)	(˚C)	(˚C/km)	(m)	(˚C/km)
LKT1	05-123-09341-0000	2292.7	71.1	77.0	12.5	28.1	1451.8	
LKT2	05-049-05000-2271	2407.0	79.4	85.7	12.6	30.3	1472.2	
LKT3	05-123-18673-0000	2333.2	92.8	98.8	12.6	36.9	1447.8	
LKT4	05-049-05000-4550	2333.2	92.8	98.8	12.6	36.9	1447.8	
LKT5	05-123-21718-0000	2261.6	73.9	79.7	12.7	29.6	1409.4	
LKT6	05-123-23370-0000	2317.7	97.2	103.2	12.5	39.1	1478.3	38
LKT7	05-123-23371-0000	2305.2	105.0	111.0	12.5	42.7	1469.1	
LKT8	05-123-25911-0000	2325.0	103.9	109.9	12.6	41.8	1426.5	
LKT9	05-123-26276-0000	2348.8	106.7	112.7	12.6	42.6	1447.8	
LKT10	05-123-26279-0000	2357.3	98.9	105.0	12.6	39.1	1444.8	

#	Well API	Depth of measurement	Measured Temperature	Corrected Temperature	T_{surf}	Geothermal Gradient	GL	Average gradient
		(m)	(˚C)	(˚C)	(˚C)	(˚C/km)	(m)	(˚C/km)
LKT11	05-123-26303-0000	2360.4	98.3	104.4	12.6	38.9	1447.8	
LKT12	05-123-26304-0000	2324.4	96.1	102.1	12.6	38.5	1447.8	
LKT13	05-123-26353-0000	2334.5	97.8	103.8	12.6	39.0	1447.8	
LKT14	05-123-26354-0000	2335.4	105.6	111.6	12.6	42.3	1450.8	
LKT15	05-123-26355-0000	2353.1	103.9	110.0	12.6	41.3	1450.8	
LKT16	05-123-26457-0000	2349.4	107.2	113.3	12.6	42.8	1447.8	

Table C 5. 9 temperature data in the Lyons.

#	Well API	Depth of measurement	Measured Temperature	Corrected Temperature	T_{surf}	Geothermal Gradient	GL	Average gradient
		(m)	(˚C)	(˚C)	(˚C)	(˚C/km)	(m)	(˚C/km)
LYO1	05-123-05150-0000	2671.3	98.3	105.2	12.7	34.6	1432.9	
LYO2	05-049-05000-1140	2368.9	98.3	104.5	12.7	38.7	1432.9	
LYO3	05-049-05000-1155	2538.4	73.3	79.9	12.8	26.4	1385.3	
LYO4	05-123-05206-0000	2662.7	106.7	113.5	12.7	37.8	1421.0	
LYO5	05-123-05306-0000	2755.4	95.6	102.7	12.4	32.7	1469.7	34
LYO6	05-123-10176-0000	2786.8	113.3	120.5	12.4	38.8	1472.2	
LYO7	05-123-11423-0000	2369.2	82.2	88.3	12.3	32.1	1492.0	
LYO10	05-123-23038-0000	2743.2	85.0	92.1	12.7	28.9	1433.2	
LYO13	05-123-26604-0000	2770.0	115.0	122.1	12.6	39.5	1435.3	

53

APPENDIX D: Operation limit calculation

In the production well, hot water flows up driven by higher pressure at the bottomhole. As fluid flows up, pressure drops due to friction loss and hydrostatic head, which might cause the hot water to flash into steam. To prevent that, a lineshaft pump will be set to its deepest possible location, to shorten the distance the water needs to flow up spontaneously. The minimum production well bottomhole pressure is calculated as follows.

Main equation: Bernoulli's equation (incompressible fluid) in terms of energy head,

$$\frac{P_1}{\gamma_w} + \frac{v_1^2}{2g} + z_1 = \frac{P_2}{\gamma_w} + \frac{v_2^2}{2g} + z_2 + h_{f2} \tag{A. 1}$$

$$\frac{P_1}{\gamma_w} + \frac{v_1^2}{2g} + z_1 = \frac{P_2}{\gamma_w} + \frac{v_2^2}{2g} + z_2 + f\frac{z_2 - z_1}{D}\frac{v_2^2}{2g} \tag{A. 2}$$

where point 1 is at the bottomhole and point 2 is at the pump location.

In order to avoid water flashing, the minimum required pressure at the pump location, P_2, is selected as the boiling pressure under water temperature of 137°C. From the National Institute of Standards and Technology (NIST) Chemistry Webbook, the boiling pressure is 0.332 MPa, and the density of water, ρ_w, is 929 kg/m³, viscosity of water, μ_w is 0.0002 Pa·s. A safety margin of 50 psig for the pump is added to the pressure at point 1, as it is the default value used in the Geothermal Electricity Technology Evaluation Model (GETEM) (GTO-DOE, 2012). So the pressure at point 2, P_2, equals 675,417 kPa.

The bottomhole depth is selected to be the deepest depth among all 12 water disposal wells to insure the required bottomhole pressure is a minimum value; and the value is 9296 ft (2833.4 m). The pump depth is 2000 ft (609.6 m). In the calculation using the Bernoulli equation, the depths are transferred into elevation. Elevation at the bottomhole (point 1), z_1, is zero. Elevation at the pump location (point 2), z_2, is 2223.8 m. The pipe roughness is 0.1 mm and the friction factor, f, is read to be 0.017 from the Moody diagram. P_1 is calculated to be 21,348 kPa and it is assigned to the minimum production well bottomhole pressure.

The maximum injector bottomhole pressure is the pressure the injector wellbore can bear without fracturing the reservoir formation. Fracture gradient for Lyons Formation sandstone is assumed to be 0.6 psi/ft.

The maximum injection well bottomhole pressure is calculated to be 35,269 kPa in the following equation:

$$BHP_{inj,\max} = FG \times D_{reservoitop}$$ (A. 3)

Dimensionless Fracture Conductivity

Dimensionless fracture conductivity is described as the product of two dimensionless variables, dimensionless relative fracture permeability (k_{fD}) and dimensionless fracture width (w_{fD}), as shown in equation (A. 4).

$$C_{fD} = k_{fD} \times w_{fD} = \frac{k_f}{k} \times \frac{w}{x_f}$$ (A. 4)

where k is the permeability of the matrix, k_f, w, x_f are the permeability, width and half-length of the fracture.

A calculation of default dimensionless fracture conductivity is shown below. The default fracture half-length, x_f, is 500 m. Real dimensionless fracture conductivity is chosen to be 1.5. The typical value in hydraulic fracture width is 0.1 in (0.00254 m). The mode value of the reservoir permeability, 7.81 md, is used for estimating the fracture permeability. Real fracture permeability has a value of 2,306,102 mD. Simulated fracture width is chosen to be 0.152 m for the simulator, so the simulated fracture permeability is calculated to be 38,536 mD, rounding to nearest 1,000 to be 39,000 mD for the default case.

Thermal breakthrough time is calculated using the following equation (Gringarten and Sauty, 1975),

$$\Delta t = \left[\phi + (1-\phi)\frac{\rho_r C_r}{\rho_w C_w}\right]\frac{\pi}{3}\frac{D^2 h}{Q}$$ (A. 5)

where D is the distance between wells in meters, Q is the volumetric injection/production well flow rate in the unit of m³/day, h is reservoir thickness in meters, ϕ is the mode reservoir porosity value, $\rho_w C_w$ is the water heat capacity in kJ/m³ °C and $\rho_r C_r$ is the rock heat capacity in kJ/m³ °C.